HHS Public Access

Author manuscript

Neuroimage. Author manuscript; available in PMC 2017 November 15.

Published in final edited form as:

Neuroimage. 2016 November 15; 142: 498–511. doi:10.1016/j.neuroimage.2016.08.014.

The Fornix Provides Multiple Biomarkers to Characterize Circuit Disruption in a Mouse Model of Alzheimer's Disease

Alexandra Badea[1], **Lauren Kane**[2], **Robert J Anderson**[1], **Yi Qi**[1], **Mark Foster**[1], **Gary P Cofer**[1], **Neil Medvitz**[3], **Anne F Buckley**[3], **Andreas K Badea**[1], **William C. Wetsel**[4], and **Carol A Colton**[5]

[1]Center for In Vivo Microscopy, Duke University Medical Center, Department of Radiology, Duke University Medical Center, Durham, NC 27710, USA

[2]Trinity College of Arts & Sciences, Duke University, Durham, NC 27710, USA

[3]Department of Pathology, and Preston Robert Tisch Brain Tumor Center, Duke University Medical Center, Durham, NC, 27710, USA

[4]Departments of Psychiatry and Behavioral Sciences, Cell Biology, and Neurobiology, Duke University Medical Center, Durham, NC 27710, USA

[5]Department of Neurology, Duke University Medical Center, Durham, NC 27710, USA

Abstract

Multivariate biomarkers are needed for detecting Alzheimer's disease (AD), understanding its etiology, and quantifying the effect of therapies. Mouse models provide opportunities to study characteristics of AD in well-controlled environments that can help facilitate development of early interventions. The CVN-AD mouse model replicates multiple AD hallmark pathologies, and we identified multivariate biomarkers characterizing a brain circuit disruption predictive of cognitive decline. *In vivo* and *ex vivo* magnetic resonance imaging (MRI) revealed that CVN-AD mice replicate the hippocampal atrophy (6%), characteristic of humans with AD, and also present changes in subcortical areas. The largest effect was in the fornix (23% smaller), which connects the septum, hippocampus, and hypothalamus. In characterizing the fornix with diffusion tensor imaging, fractional anisotropy was most sensitive (20% reduction), followed by radial (15%) and axial diffusivity (2%), in detecting pathological changes. These findings were strengthened by optical microscopy and ultrastructural analyses. Ultrastructual analysis provided estimates of axonal density, diameters, and myelination—through the g-ratio, defined as the ratio between the axonal diameter, and the diameter of the axon plus the myelin sheath. The fornix had reduced axonal density (47% fewer), axonal degeneration (13% larger axons), and abnormal myelination (1.5% smaller g-ratios). CD68 staining showed that white matter pathology could be secondary to neuronal degeneration, or due to direct microglial attack. In conclusion, these findings strengthen

Correspondence: Alexandra Badea, PhD, Box 3302 Duke University Medical Center, Durham, NC, 27710, USA, Tel: +1 919 684-7654, alexandra.badea@duke.edu.

the hypothesis that the fornix plays a role in AD, and can be used as a disease biomarker and as a target for therapy.

Graphical Abstract

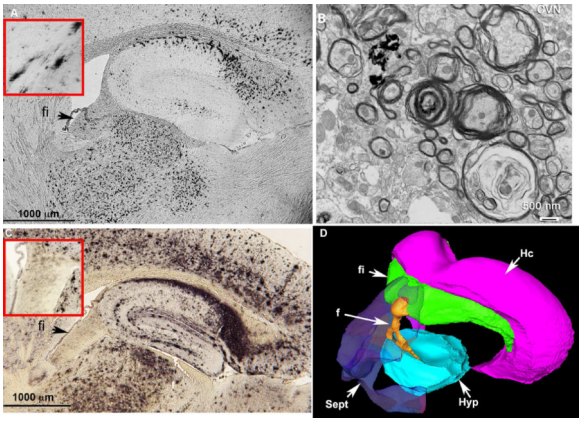

One line summary

White matter changes in the fimbria/fornix play a role in the progression of AD, and can be used as a biomarker of disease, and as a target for therapy

Keywords

Alzheimer's disease; diffusion tensor imaging; electron microscopy; fornix; mouse models

Introduction

An estimated 5.3 million Americans, including 11% of people over age 65, are afflicted with Alzheimer's disease (AD) (Alzheimer's Association, 2015). This number is expected to escalate, as the proportion of older Americans continues to increase. Unfortunately, the cause of this neurodegenerative disorder is not fully understood, and no therapy has been successful in arresting, or reducing the pathology associated with AD.

The hallmarks of AD include cognitive deficits, amyloid plaques, neurofibrillary tangles, and neuronal loss (Braak et al., 1993). Morphometric brain changes in the medial temporal lobe (in particular the hippocampus) and neocortex are among the early imaging markers detected by MRI (Wisniewski et al., 1985; Jack Jr et al., 1997; Jack Jr et al., 1999; Yoshiyama et al., 2007). Such MRI-based markers of neurodegeneration have been proposed as predictors of conversion from mild cognitive impairment to AD (Kantarci et al., 2009). It has been proposed that white matter also plays a role in the progression of pathology, as AD patients show myelin degradation (Brun and Englund, 1986; Bartzokis et al., 2003; Bartzokis, 2004). Even presymptomatic carriers of familial AD have shown changes in late myelinating fibers connecting limbic structures, such as the fornix. These changes can be related to memory impairment and have predictive value (Ringman et al., 2007; Parra et al., 2015).

Mouse models provide useful tools for dissecting the relationship between white matter abnormalities and other pathologies, such as amyloid deposition (Song et al., 2004; Sun et al., 2005; Müller et al., 2013; Sun et al., 2014), abnormal tau hyperphosphorylation (Wells et al., 2015), vascular damage (Pathak et al., 2011), and the immune response (Tan et al., 1999; Frodl and Amico, 2014). To help understand the pathology and progression of AD, we have chosen to study the *APPSwDI*$^{+/+}$/*mNos2*$^{-/-}$ (CVN-AD) mouse strain because it recapitulates multiple aspects of the human AD pathology, well described in previous publications (Wilcock et al., 2008; Colton et al., 2014; Kan et al., 2015). The CVN-AD mouse expresses the Swedish, Dutch, and Iowa mutations of the human amyloid precursor protein gene (APP) on a murine nitric oxide synthase 2 knockout background (*mNos2*$^{-/-}$) (Colton et al., 2006; Colton et al., 2014). Deletion of the murine *Nos2* gene was used to better mimic human immunity, where immune-activated *NOS2* expression and *iNOS* production are significantly reduced compared to rodents (Weinberg et al., 1995; Guo et al., 2012; Hoos et al., 2014). CVN-AD mice show amyloid deposition (beginning at 6 weeks of age, particularly around blood vessels); hyperphosphorylated and aggregated mouse tau (24 weeks); deficits in memory and learning (24 weeks); and neuronal degeneration and loss (36 weeks) (Wilcock et al., 2008; Colton et al., 2014). Multiple inflammatory changes, including altered microglial activity, were also observed in CVN-AD mice (Kan et al., 2015). Activated microglia have been implicated in promoting neurodegeneration (Akiyama et al., 2000; Schott and Revesz, 2013), as well as axonal and myelin damage (di Penta et al., 2013). We therefore hypothesized that CVN-AD mice replicate the hippocampal atrophy observed in humans with AD, as well as the associated reduced white matter integrity.

MRI has been shown to be particularly suitable for quantifying morphometric and microstructural changes in mouse models of neurological conditions (Benveniste et al., 2007), and such changes can be reported using MR-specific reference brain atlases with high-resolution anatomical mapping (Kovačević et al., 2005; Badea et al., 2007; Aggarwal et al., 2010; Ullmann et al., 2015). Our objective was to quantify the impact of amyloid accumulation, vascular changes, and inflammation on the neuroanatomy of the CVN-AD mouse, compared to age-matched *mNos2*$^{-/-}$controls, using imaging at multiple resolution levels. Our hypothesis was that *in vivo* MRI, and high-resolution diffusion tensor imaging (DTI) would locate areas with significant changes in regional volumes and DTI parameters. This should identify vulnerable brain regions, as well as the circuits connecting them, and we expected that primary candidates would be components of the septo-hippocampal circuit. We also sought to understand the underlying causes for DTI changes using histological and ultrastructural imaging. The demonstration of white matter abnormalities in the CVN-AD mouse model, in tracts relevant to AD, would support that changes in white matter have an important role in AD, and potential predictive value, suggesting that white matter protection and repair may provide valid therapeutic targets (Oishi and Lyketsos, 2014; Douet and Chang, 2015).

Materials and Methods

Animals

Homozygous *APPSwDI/mNos2*$^{-/-}$ (CVN-AD) mice were produced by crossing mice expressing the Swedish K760N/M671L, Dutch E693Q, and Iowa D694N human *APP* mutations under control of the Thy-1 promoter (Davis et al., 2004) with *mNos2*$^{-/-}$ (B6 129P2Nos2^{tau1Lau}/J) mice (Laubach et al., 1998) (Jackson Laboratory stock number 002609, Bar Harbor ME). Dr. William Van Nostrand and Judianne Davis at Stony Brook University Medical Center generously provided *APPSwDI* mice used in this study. To reduce litter bias as a factor in our analyses, young mice from each genotype used in the experiments were ear tagged at weaning, assigned a random number and then placed into cages with 4 other weaned mice of the same sex, also designated for the experiments. Raising the mice together in this manner, assured that randomly selected cage mates were from different genotypes and subjected to the same environmental and social conditions (Shineman et al., 2011). All mice were genotyped using standard PCR. Mice were bred through the barrier colonies at Duke University, fed standard mouse chow ad libitum, and housed under 12-hour light/12-hour dark cycles, at 21±3°C.

The AD-like pathological phenotype of the CVN-AD mice include the following characteristics: 1) mutated human APP is not overexpressed but is approximately 0.7-fold of the normal mouse APP level (Miao et al., 2005); 2) Aβ deposition resulting from expression of the SwDI mutations in APP occurs first around blood vessels and an apparent failure to clear Aβ from the brain, which is similar to humans with cerebral amyloid angiopathy (CAA) (Attems et al., 2010); 3) CVN-AD mice show AT8 antibody immunopositive hyperphosphorylated tau (Colton et al., 2014), and the subsequent tau pathology is not dependent on mutated human tau genes that do not represent AD (Oddo et al., 2003); 4) the mutated human APP (APPSwDI) gene is expressed on a *Nos2*-deficient background, resulting in a pheno-copy of low human immune-based NO production; and 5) significant neuronal loss and synaptic changes in the brain are observed beyond 36 weeks of age, but not at 12 weeks (Colton et al., 2014). In contrast other studies have observed early on differences in the pathology of mouse brains (Allemang-Grand et al., 2015), underlying the importance of accounting for developmental confounds.

To establish our MRI analyses as useful for detecting brain pathological parameters, we used mice between a lower age limit of 14–15 months and an upper limit of 18 months. These ages represent the transition between middle age and senescence, and were chosen to represent an age where biomarkers of age and full expression of AD-like pathology were evident in each mouse but were not representative of senescence (Fox, 2007). The MRI study thus included 9 *APPSwDI/mNos2*$^{-/-}$ (CVN-AD) and 8 *mNos2*$^{-/-}$ controls, aged 14–18 months, of mixed genders (3 CVN-AD males and 6 females; 4 *mNos2*$^{-/-}$ male controls and 4 females). One female *mNos2*$^{-/-}$ was excluded from the DTI analysis, because of anommalous estimates of tensor derived parameters. All animal procedures were conducted according to the NIH Guide for the Utilization and Care of Vertebrate Animals Used in Testing, Research and Training, and approved by the Institutional Animal Care and Use Committee of Duke University Medical Center.

MR Imaging

In vivo MRI of mouse brains was conducted using a 7T, 20-cm bore magnet (Bruker BioSpec 70/20 USR, Billerica, MA) interfaced to an Avance III system. The scanner has actively shielded gradients with integrated shims up to 2nd order. We used a 114 mm inner-diameter insert gradient coil, which can supply 450 mT/m, with a rise time of 110 μs, and a quadrature radio frequency (RF) transmit-receive cryogenic coil.

Mice were maintained under isoflurane anesthesia (1.2 ±0.5%) throughout imaging, which consisted of a rapid acquisition with relaxation enhancement (RARE) protocol with a repetition time (TR) 1.8 s, effective echo time (TE) 28.3 ms, echo spacing 9.4 ms, RARE factor 8, field of view 20×15x13 mm, matrix 200×150x130 voxels, bandwidth 50 kHz. Images were reconstructed at 100 μm isotropic resolution, and acquisition time was ~1 hour.

For *ex vivo*, high-resolution diffusion tensor imaging (DTI), we prepared actively stained mouse brain specimens, similar to (Johnson et al., 2007). The animals were anesthetized to a surgical plane and perfused through the left ventricle, with outflow from the right atrium. Saline (0.9%) was used to flush out the blood, at a rate of 8 ml/minute, for 5 minutes. Fixation was carried out by perfusing with a 10% solution of neutral buffered formalin phosphate containing 10% (50 mM) Gadoteridol (ProHance, Bracco Diagnostics Inc., Monroe Township, NJ), at a rate of 8 ml/minute for 5 minutes. Gadoteridol reduced the spin lattice relaxation time (T1) of tissue to ~100 ms, providing significant signal enhancement (Johnson et al., 2002). Mouse heads were stored in 10% formalin for 24 hours. Finally, the fixed specimens were transferred to a 0.01 M solution of phosphate buffered saline (PBS) containing 0.5% (2.5 mM) Gadoteridol, at 4 °C for 5 –7 days to rehydrate the tissue. Extraneous tissue around the cranium was removed prior to imaging, and specimens were placed in MRI-compatible tubes, immersed in perfluoropolyether (Galden Pro, Solvay, NJ) for susceptibility matching.

Fixed specimens were scanned on a 9.4 T, 8.9 cm vertical bore Oxford magnet, with shielded coils, providing gradients up to 2000 mT/m (Resonance Research, Inc. Billerica, MA), and controlled by an Agilent Direct Drive Console (Agilent Technologies, Santa Clara, CA). The DTI protocol used 12 diffusion directions, and TE 12 ms, TR 100 ms, b ≈ 1595 s/mm^2, diffusion pulse width 4.04 ms, separation 5 ms, amplitude 90.94 G/cm). Images were acquired over a 22×11x9.02 mm field of view, with a matrix 400×200x164, and reconstructed at 55 μm isotropic resolution. Specimens were scanned within the cranium to avoid tissue damage and distortions. The scan duration was ~12 hours.

Myelin Staining

For myelin staining, we used a separate cohort, including 4 CVN and 4 *mNos2*$^{-/-}$ mice, aged 36.13±1.73 weeks. Mice were perfused with saline, the brains removed, and a hemisphere was fixed in formalin for 24 hours. 25 mm thick sections were cut using a freezing microtome, and placed on slides to dry overnight. Slides were rinsed in 95% ethanol (EtOH) and placed in 1% luxol fast blue (LFB) overnight at 60°C. Slides were then rinsed in 95% EtOH, submerged in dH2O for 5 minutes, followed by 0.05% lithium carbonate for 1 minute. Staining was differentiated by placing the slides in 70% EtOH for 30

seconds, followed by rinsing in dH2O, and dipping in eosin to counterstain for 21 seconds. Slides were rinsed in 70% EtOH until the desired eosin contrast, ~30 s per slide. Lastly, sections were dehydrated with a series of EtOH steps (3 min in 75% EtOH, 3 min in 95% EtOH, 3 min in 100% EtOH, 5 min in 100% EtOH, 2 × 5 min xylene), and mounted with xylene media.

An LSM 510 Meta microscope (Carl Zeiss Microscopy, LCC, Thornwood, NY) was used for imaging slides using a 10× objective (Zeiss W Plan-Apochromat, NA 1.0).

Transmission Electron Microscopy

After MR imaging of actively stained brains, two specimens from each genotype were immersed in 4% gluteraldehyde for one week, extracted from the skull, hemisected along the mid-sagittal line, and sliced using a vibratome. Sections were treated with 2% osmium tetroxide, dehydrated through successive acetone baths, infiltrated with Epoxy 812, flat embedded, and polymerized. Corresponding areas of the fornix for each specimen were mounted onto resin blocks, to provide horizontal sections. The location for the fornix specimens was immediately superior and caudal to the anterior commissure, identified by horizontal plane −3.96 mm from bregma, 0.3 mm lateral from the mid-sagittal plane, −0.2 mm caudal to bregma, and corresponded to plate 145, and its neighbors 144–146 from (Paxinos and Franklin, 2013). Ultrathin (70 nm) sections were cut, gathered onto grids, and stained with uranyl acetate and lead citrate. Grids were imaged using a Philips CM-12 system, at 7100 magnification.

Immunohistochemistry

After injection with a lethal mixture of ketamine/xylazine (260 mg/kg ketamine/ 20 mg/kg xylazine), mice were intracardially perfused with 25 ml of PBS to remove intravascular blood cells. Perfused brains were then rapidly removed, bisected in the mid-sagittal plane, and the right hemisphere was placed into 4% paraformaldehyde overnight for fixation. Fixed brains were cryoprotected by sequential passage through 10%, 20%, and 30% sucrose for 24 hours, followed by sectioning using a freezing microtome into 25 μm sagittal sections. Sections from CVN-AD and control mice were immunostained with standard techniques using either: 1) an anti-CD68 antibody (Clone FA-11; AbD Serotec; Raleigh NC); 2) an anti-GFAP antibody (13–0300; Zymed-Invitrogen); or 3) an anti-beta amyloid (H31L21; Life Technology, Grand Island, NY; specific to Amyloid β1–42; *not* Amyloid β1–40, Amyloid β1–43, Amyloid β1–37 or Amyloid β1–38). Secondary antibodies, ABC, and DAB kits were purchased from Vector Laboratories (Burlingame, CA).

Image Analysis and Statistics

Image analysis was similar for both *in vivo* and *ex vivo* MRI-based morphometry, with the difference that *in vivo* MRI required reducing the effects due to B_1 field inhomogeneities, from the cryogenic surface coil. For this purpose, we applied a bias field correction (N4ITK) method (Tustison et al., 2010) implemented within the Advanced Normalization Tools package (ANTs) (Avants et al., 2008; Avants et al., 2014). While this was not deemed necessary for *ex vivo* images, these data were processed by co-registering individual diffusion-weighted images to the B0 image to correct for Eddy distortions, using a 12

degrees of freedom (dof) affine transform and ANTs. Subsequent diffusion tensor calculation was performed using the Diffusion Toolkit (Wang et al., 2007) (http://trackvis.org), as in (Calabrese et al., 2013).

To evaluate regional differences in the neuroanatomy and DTI parameters between CVN-AD mice and controls, we used a segmentation pipeline (Badea et al., 2012) translated into a high-performance computing environment. We wrote Perl modules to parallelize pairwise registrations and perform voxel-based analysis on a 7-node cluster, managing SLURM jobs using Bright Cluster Manager.

ANTs was used for registration of fractional anisotropy (FA) images, to generate minimum deformation templates (MDT), to map all DTI parametric images into the MDT space, and to map atlas labels onto individual brains. We used a second-generation atlas (http://www.civm.duhs.duke.edu/waxholmspace2) of the mouse brain, based on (Johnson et al., 2010), to provide priors for automated segmentation of 101 regions.

To estimate myelination, we used ImageJ https://imagej.nih.gov/ij/ (Schneider et al., 2012) to measure the mean intensity of four regions of interest (ROIs) in LFB-stained slides: the anterior commissure (ac), corpus callosum (cc), fimbria (fi) - part of the fimbria-fornix system, and cortex (Cx). The ROI manager and the freehand tool were used to define the ROIs and measure their mean intensities. To compensate for variations in staining, each measurement was normalized relative to a circular region in the cortex of each animal, on a per slide basis: 100* (ROI-Cx)/Cx.

Axon numbers and diameters, as well as g-ratio estimates (defined as the ratio between the axonal diameter and the diameter of the axon plus the myelin sheath) of axonal myelination, were obtained from TEM images. We used in-house developed software and the Neural Networks toolbox in MATLAB (MathWorks, Natick, MA), trained to identify axons based on 11 morphometric features: area, eccentricity, equivalent diameter, Euler number, extent, filled area, major and minor axes length, orientation, perimeter, and solidity. The g-ratios were obtained by dividing distances from the axons' centroids to the nearest edge points in the distance maps, and located within 20% of the radius of the equivalent circles.

We used MATLAB to compute ROI statistics for: a) MRI based estimates of volume and diffusion tensor parameters; b) LFB contrast estimates; c) electron microscopy (TEM) parameters, including axonal numbers, diameters; and g-ratios. Regional statistics used two-tailed t tests, $p<0.05$, 15 degrees of freedom for MR measurements, 67 degrees of freedom for TEM, and 6 for LFB.

For voxel-wise analysis, all DTI images were mapped into the space of the minimum deformation template, and smoothed with a 200 μm kernel. SPM 12 (Worsley et al., 1992; Friston et al., 1994) was used for voxel-based statistics, following a two-step approach, where uncorrected statistics were considered significant at $p<0.05$, and the minimum cluster size was 200 voxels. Multiple comparison corrections used false discovery rate and considered either: a) all voxels contained within the brain mask, or b) voxels with fractional anisotropy values >0.3, to focus on white matter. We chose a conservative FDR = 5% threshold for the *ex vivo* data. We relaxed the threshold to 10% for the *in vivo* data, because

the FDR correction becomes more conservative as correlations increases, and for smoother data (Genovese et al., 2002).

Avizo (FEI, Burlington, MA) was used for visualization of statistical parametric maps overlaid on the average fractional anisotropy image generated by *mNos2* $^{-/-}$ controls.

Results

In-vivo MR-based morphometry

In vivo MRI voxel-based analysis detected volume loss (FDR 10%, cluster size threshold 200 voxels) in top candidate areas including the septofimbrial complex, fornix, and hippocampus; in the ventral tegmental area, substantia nigra, and retorubral field; as well as the accessory olfactory areas, thalamic nuclei (anterior ventral, ventro-lateral, and reuniens), superior colliculus, and basal ganglia, with clusters extending over the internal capsule. Conversely, the lateral ventricles, and specific areas of the cortex and cerebellum were expanded (Fig. 1). A statistical threshold relaxed to $p< 0.01$ revealed more areas where CVN-AD mice were different than controls. Extended regions of atrophy were found in the hippocampus, the medio-prefrontal cortex (areas 24a/b, which project to entorhinal cortex), the paraventricular and interanteromedial thalamic nuclei, and the area 29 of the retrosplenial cortex. This latter region shows the earliest metabolic decline in AD, as measured with PET (Minoshima et al., 1997; Villain et al., 2008). On the other hand, the lateral ventricles were enlarged – indicating potential loss of tissue around the ventricles, while additional areas showed increased volume (S1 areas, amygdala (basomedial), and cerebellum) (Supplementary Fig 1).

Ex-vivo MR-based morphometry

To overcome limitations imposed by *in vivo* imaging onto resolution and contrast, we imaged the CVN-AD mouse *ex vivo* using Gadoteridol to enhance the MRI signal. The voxel-wise statistics for the deformation fields (Fig. 2 A) revealed significant volume loss in CVN-AD mouse brains in the hippocampal formation, including the stratum lacunosum moleculare and radiatum of CA1, the dentate gyrus (dorsal hippocampus), and CA3 in ventral hippocampus. Decreased volumes were also seen in the subiculum, the (ventral) hippocampal commissure, the olfactory areas, preoptic hypothalamus, lateral amygdala, lateral and triangular septum, septofimbrial nucleus, ventral thalamic nuclei, superior colliculus, and pons. Among white matter tracts, reduced volume was noted in the fornix and internal capsule. Enlarged volumes were found in areas of the neocortex, including the somatosensory cortex, corpus callosum (medially, and periventricular), dorsal thalamus, basomedial amygdala, cerebellum, and the lateral reticular nucleus. Thus, the CVN-AD mouse replicates the reduced hippocampus and subiculum seen in human AD (Bateman et al., 2012), and supports the hypothesis that the fornix plays an important role in AD.

A region-of-interest analysis showed that the difference in overall brain volumes between CVN-AD mice and age-matched *mNos2*$^{-/-}$ controls averaged 5.7%, CVN-AD (493.72±23.50 mm^3) being larger than controls (467.07±16.42 mm^3), $p=0.03$. But this difference did not survive a 5% FDR correction. After normalizing to total brain volume,

multiple gray matter regions presented significant volume differences (Supplementary Table 1, Fig. 2 B). CVN-AD mice showed significant regional volume loss in the: hippocampus, piriform cortex, hypothalamus, preoptic areas, as well as thalamic nuclei (subthalamic, reticular, and ventral nuclei, and zona incerta). Beyond the forebrain, significant volume reductions were localized in the superior colliculus, deep mesencephalic nuclei (red nucleus), vestibular nuclei, raphe nuclei, pons, and even deep cerebellar nuclei (dentate and interposed). Gray matter loss in CVN-AD mice ranged from 16.9% for the trigeminal motor nuclei, 9.6% for the raphe nuclei, ~8% for the dentate and interposed cerebellar nuclei, 7% for the piriform, >6% for hippocampus and subthalamic nucleus, and 5% for hypothalamus. The most significant white matter volume reductions occurred in the fornix (−23%). Other white matter tracts with reduced volume included the mamillothalamic tract (−11%), the fasciculus retroflexus, brachium of the superior colliculus (−9%), cerebral peduncle (−5%), and the ventral hippocampal commissure (−7%). Substantia nigra, the bed nucleus of stria terminalis, and the internal capsule showed a trend ($p<0.1$). On the other hand, volume increases were noted in the nucleus accumbens (9.8%), cortex (5.2%), ventral pallidum (7.8%), and corpus callosum (7.9%). Supplementary Fig 2 shows regions where volume differences between CVN-AD and control mice reached significance. In general, the pattern of atrophy in CVN-AD mice resembled that observed in humans with AD, particularly in the hippocampus (Jack et al., 1999; Xu et al., 2000), and its associated fornix (Copenhaver et al., 2006).

DTI identifies multiple microstructural alterations in CVN-AD

The fractional anisotropy (FA) statistical maps revealed that the regions surviving FDR corrections (5%) were restricted to the fornix and ventral thalamic nuclei when all brain voxels were included in the analysis (Fig. 3 A). However, when we asked the question "where does white matter change?" constraining *a priori* the analysis to voxels where FA>0.3, then areas of the corpus callosum, internal capsule (ic), cerebral peduncle (cp), and middle cerebellar peduncle (mcp) were also detected to change. Importantly, the regional analysis for DTI parameters showed that most white matter tracts (except for stria terminalis) had reduced FA in CVN-AD mice (Fig. 3 B), indicating reduced white matter integrity. Regional analysis identified the largest effect in the fornix, where FA was 20% lower. FA reduction was also observed in the ventral hippocampal commissure (−9.3%), internal capsule (−10.2%,), cerebral peduncle (−6%,), as well as the pyramids (−11.4%), corpus callosum (−5.4%), anterior commissure, and middle cerebellar peduncle (−3%). Gray matter areas with reduced FA included the ventral thalamic nuclei (−13.4%), the pontine nuclei (−6%) and hypothalamus (−9.5) (Fig. 3 C).

Uncorrected voxel-wise changes (Supplementary Fig 3) in diffusion tensor parameters, including axial diffusivity (or primary eigenvalue, E1), and fractional anisotropy (FA), showed reductions in CVN-AD mice; while radial diffusivity (RD) and apparent diffusion coefficient (ADC) were increased. E1 was reduced in the dorsal fornix, hippocampal commissure; as well as the internal capsule, cerebral peduncles, lateral lemniscus, middle cerebellar peduncles, and deep cerebellar white mater. FA was reduced in the corpus callosum, hippocampal commissure, internal capsule, external medullary lamina (lateral to the ventral thalamic nuclei, and medial to the reticular thalamic nuclei), the longitudinal

fasciculus of pons, fornix, anterior commissure, cerebral peduncles, and pyramids. Voxel-wise changes in axial diffusivity (E1) showed similar reduction patterns with FA. The secondary eigenvalue (E2), radial diffusivity (RD), and apparent diffusion coefficient (ADC) were increased in CVN-AD mice in areas of the corpus callosum (genu), septofimbrial nucleus, lateral septal nucleus, fimbria, and fornix, ventral hippocampal commissure, fornix (RD only), and pyramids (RD).

We examined separately the orthogonal E1 and E2 eigenvalues, as well as RD. The brain regions showing significant differences are included in Fig. 4 and in Supplementary Table 2. Reductions in E1, suggestive of lower axonal density, were found in the optic tract (−7.5%,), cerebral peduncle, the 8th nerve (−6%), middle cerebellar penduncle (−6.8%), and ventro-spino-cerebellar tract (−4.7%). The reverse was noted for stria terminalis (7%). Increases in RD, suggestive of damaged myelin, were found in the fornix (14%), ventral hippocampal commissure (11%), as well as the pyramids (18%) and pontine nuclei (5%). A trend was found for the corpus callosum, brachium of the superior colliculus (>7%), the anterior commissure, and fimbria (>10%). E2 was significantly larger in the fimbria and ventral hippocampal commissure (>10%,). ADC differences were found in the ventral hippocampal commissure (6.9%) and stria terminalis (7.4), while fimbria and fornix (>6%) showed a trend. By identifying anatomical structures that showed significant changes in multiple parameters (volume and DTI), we have defined a set of vulnerable regions of interest in CVN-AD mice that include the fornix, ventral hippocampal commissure, fimbria, corpus callosum, and cerebral peduncle.

A salient feature in CVN-AD mice based on MR imaging was related to the fornix, characterized by decreased volume, and altered DTI properties. We fitted a linear model of the fornix FA as a function of the hippocampal volume, and found that hippocampal volume predicts the fornix FA, $R^2 = 0.6$, F=22.7, p=0.00025, versus a constant model (T=4.76 for fornix FA coefficient, df=15).

Reduced myelination

To better understand the biological underpinning for the microstructural changes estimated through DTI parameters (such as fractional anisotropy, FA) we used bright field microscopy to image LFB stained brain slices from CVN-AD and age-matched *mNos2*$^{-/-}$ control mice. The contrast between white matter and cortex was reduced in CVN-AD mice for all regions measured (anterior commissure, corpus callosum, and fimbria), but only the fimbria reached significance at $p<0.05$, and 8.3% lower contrast (Fig. 5). MR images through similar sections indicated areas of reduced fractional anisotropy in the corpus callosum, the fimbria-fornix, and the peripheral area of the anterior commissure ($p<0.05$). The LFB thus detected reduced myelin in the fornix, which is consistent with the FA decrease detected by DTI.

Ultrastructural alterations

We used electron microscopy to further examine white matter areas with the most prominent changes identified using DTI and LFB (Fig. 6). The ultrastructural images of the fornix showed: a) lower density of myelinated axons (49±14 axons/field, or 0.59±0.17 axons/μm^2 in CVN-AD mice; versus 94±20 axons/field, or 1.12±0.24 axons/μm^2 in *mNos2*$^{-/-}$ mice,

p=5.5*10^{-16}, CI=[-52.83, −36.10] (see Supplementary Fig 4); b) increased variation in size and shape (average axon diameters 702±86 μm in CVN-AD mice, versus 620.26±44.01 μm in controls, p=4.6*10^{-5}, ci=[12.65; 34.05]; c) features of degeneration (lysosomal material, dark axoplasm, vacuolation). G-ratios were different than the ideal 0.6 in both genotypes, averaging 0.80±0.02 in CVN-AD mice, versus 0.78±0.02 in *mNos2*$^{-/-}$ in controls—a small, but significant difference, p<0.01, ci=[0.003,0.021]. This differences is possibly due to the old age of these mice.

We noted the presence of swollen, dystrophic axons, and distorted myelin sheets, myelin balloons and vacuole, as well as dark or lucent inclusions, and lipid deposits. Some inclusions were lamellar, probably myelin residues. These were observed predominantly in CVN-AD mice, and to a lesser extent in *mNos2*$^{-/-}$ mice. Microglia were also noted in both animals, with a larger presence in CVN-AD mice. The most prominent features for fornix were reduced axonal density and nonuniform axon sizes.

Microglial involvement in SHH circuit pathology

To better understand the involvement of microglia in the apparent damage to the hippocampus and its connecting fibers in CVN-AD mice, we immunostained fixed brain sections with CD68 antibodies, to identify phagocytic processes and the uptake of oxidized lipoproteins (Ottnad et al., 1995; Ramprasad et al., 1996). Prominent CD68 positive cells were observed in the subiculum, hippocampus, and fimbria in CVN-AD mice (Fig. 7 A), but not in *mNos2*$^{-/-}$ controls (Fig. 7 B). In addition to microglia, GFAP- positive astrocytes were also located in and around myelinated regions in both CVN-AD and *mNos2*$^{-/-}$ brain sections, with more staining in CVN-AD mice (Fig. 7 C and D). An increase in GFAP immunostaining and levels of GFAP protein with age in the hippocampus and cortex of CVN-AD mice compared to control mice has been previously noted (Hoos et al., 2013). Thus, astrocytes as well as microglia may contribute to the pathological changes in these brain areas. In contrast, Ab immunostaining using the H31L21 antibody (Life Technology, Grand Island, NY) was localized primarily in gray matter areas (Fig. 7 E). Together, these findings suggest active involvement in phagocytic processes within myelinated areas of the septo-hippocampal-hypothalamic circuit in CVN-AD mice (Fig. 7 F).

Summary

We identified significant neuroanatomical differences in the CVN-AD mouse model relative to age-matched *mNos2*$^{-/-}$ controls, using techniques spanning multiple resolution scales, including MRI, DTI, histological staining, immunohistochemistry, and transmission electron microscopy (TEM). MR/DTI atlas-based regional segmentation and voxel-wise analyses identified vulnerable regions, in both gray and white matter, based on differences in morphometry and water diffusion properties. White matter specific differences, detected by MR and multiple DTI parameters, were significant in the fimbria/fornix myelinated axons, and were explained by histological (luxol fast blue and immunohistochemistry), and ultrastructural imaging findings. We conclude that the most prominent image based phenotypes, for the CVN-AD mouse, involved a brain circuit that includes the septum, hippocampus, fimbria and fornix, as they connect to the hypothalamus (Fig. 7 F).

Discussion

Longitudinal studies in presymptomatic carriers of high genetic risk mutations have revealed evidence of biomarker changes which may precede clinical AD symptoms by more than a decade (Sperling et al., 2011). These changes include brain atrophy (Jack et al., 2015), fMRI abnormalities (Dickerson et al., 2005) (Sperling, 2007), FDG PET hypometabolism (Gallivanone et al., 2016), and Aβ accumulation (Vos et al., 2016). Preventive strategies and pharmacological approaches targeting circuits at such early stages will provide unique opportunities to test interventions when the window of opportunity is optimal for success.

It is thus critical to develop sensitive methods for early detection of changes in AD biomarkers, both for understanding the pathogenesis of AD, and for monitoring disease-modifying interventions. MRI has been used to detect early atrophy throughout the brains of AD patients, in particular in the medial temporal lobe gray matter (Jack et al., 1997; Eskildsen et al., 2015). White matter changes have also been described in AD (Brun and Englund, 1986; Bozzali et al., 2002; Ihara et al., 2010). The fornix, connecting the medial temporal lobe to the hypothalamus, is particularly susceptible and shows early changes in AD. Moreover, fornix integrity has been associated with diagnostic classification, cognitive changes, and response to therapy (Nowrangi and Rosenberg, 2015).

We have used MR-DTI, as a sensitive diagnostic tool, to detect neuroanatomical and microstructural changes in a mouse model of AD, under the hypothesis that mouse models, although controversial, provide unique opportunities to study aspects of AD pathology. Our goal has been to quantify structural changes, and we found salient features in the septo-hippocampal-hypothalamic (SHH) circuitry of the CVN-AD mouse using a multi-scale, multi-modal imaging approach. We identified volumetric changes using *in vivo* MRI, then confirmed and expanded these findings using *ex vivo* DTI, which added orthogonal perspectives on tissue microstructure. DTI revealed that gray matter changes are accompanied by alterations in white matter connecting the SHH circuitry. Differences were most prominent in the fimbria/fornix and the hippocampal commissure, and linked to abnormal axonal density and myelination through histological and ultrastructural imaging. In addition, we noticed changes in radial diffusivity and the apparent diffusion coefficient (Suppl. Fig 3, A and C) in periventricular regions (where microglia are also observed to accumulate, data not shown), and in the corpus callosum.

Our results confirmed that CVN-AD mice model neuropathological aspects of AD, and in particular, show changes in the SHH circuit linked by the fornix. Despite the low resolution of *in vivo* MRI, the fornix emerged as having a strong phenotype, being smaller in CVN-AD mice. MR-based morphometry from *ex vivo*, Gadolinium stained brain specimens, strengthened the *in vivo* finding, and provided higher precision and significance (FDR 5%). The olfactory areas, hippocampus, septofimbrial nucleus, anteroventral thalamus, substantia nigra, and ventral tegmental areas, as well as the striatum were reduced. As shown previously for other amyloid mouse models, we found enlarged volumes in some areas of the brain, for example the somatosensory cortex, cerebellum, and areas of the corpus callosum. This type of change has been observed in multiple mouse models of AD including the TgCRND8 (Allemang-Grand et al.), APPJ20 (Grand'Maison et al.), PSAPP and ArcAβ

(Grandjean et al., 2016), and are generally in contrast to the pathology commonly observed in AD patients. AD is associated with cortical thinning and cortical volume loss (Ewers et al., 2011). However, heterogeneity has been demonstrated in human studies. Non-linear volume changes are observed in APOE4 positive AD patients where increased volumes can be observed particularly early in disease (Gispert et al., 2015). Whole brain, cortical, and hippocampal volume increases due to APP or PS1 transgenes have been reported in humans and have been attributed to amyloid deposition (Fortea et al., 2010), gliosis (Beach et al., 1989), increased extracellular space, cellular swelling in response to toxicity, or to a compensatory mechanism (Iacono et al., 2008). Clearly, the heterogeneity of differences in pathway complexity and timing of pathological events between mouse models of AD and humans with AD makes us well aware that mouse models, as many other approaches used to understanding the underlying mechanisms of AD, have limitations.

While morphometric results in mouse models of AD have been mixed, possibly because of competing effects between neurodegeneration, amyloid deposition, and astrogliosis (Ka¨rkka¨inen et al., 2015), our results fit an emerging pattern of early damage to white matter and regional circuitry resembling human AD pathological changes. Using voxel-wise analysis, we have now identified additional susceptible areas, including the olfactory areas, anterior hypothalamus, lateral amygdala, and ventral thalamic nuclei, as well as dorsal subiculum, CA1 and CA3 hippocampal areas. The hippocampal volume reduction is consistent with findings in APP/TTA (Jankowsky et al. 2005) (Badea et al. 2010), APP/PS1 mice (Lau et al. 2008), APP/SOD1 (Borg and Chereul 2008), and Tg4510 (Yang et al. 2011) (Wells et al. 2015) mice. But hippocampal atrophy is not a universal finding in mouse models of AD, and multiple models including APP/PS1, E22ΔAβ and ArcAβ show either no change or increased volume in this critical brain region (Grandjean et al., 2016). In addition to hippocampal volume changes, CVN-AD mice presented MRI atrophy of white matter tracts including the fornix, hippocampal commissure, and internal capsule in both *in vivo* and *ex vivo* conditions. To better understand the substrate for white matter changes we adopted a multivariate approach, including DTI parametric analysis, knowing that high FA and E1, but low ADC and RD are associated with healthy white matter. The DTI analysis revealed substantial effects in CVN-AD mice. FA decreased and RD increased in the fornix and hippocampal commissure while increased secondary eigenvalue (E2) of the diffusion tensor further established deficits in the fimbria. Our investigation of the ability of multivariate DTI parameters to locate areas with altered microstructure found the largest effect for the fornix where a 20% decrease in FA, followed by a 15% increase in RD, were observed. Smaller changes in E2 (8%) and E1 (2%) were not significant in these brain regions. E2, however, captured changes in the fimbria and hippocampal commissure (~10%), while E1 detected a 7% decrease for fimbria. We observed a 9% decrease in FA for the hippocampal commissure. These differences may indicate different sensitivities of DTI parameters to microstructural alterations, as well as limitations in detecting focal changes using regional measures.

Our results herein not only complement but also add to the existing literature. A limited number of AD mouse models have been characterized with DTI, and most have used a region of interest (ROI) approach and models of cerebral amyloidosis (Song et al., 2004; Sun et al., 2005; Harms et al., 2006; Qin et al., 2013); while others have used whole brain

voxel-based analysis to study models of tau pathology (Wells et al., 2015). A recent comparative study (Grandjean et al., 2016) showed significant increased FA in the minor forceps of the ArcAβ model with no similar changes in the PSAPP or E22ΔAβ strains and decreased FA in the external capsule of PSAPP mice with no change in the corresponding regions from E22ΔAβ or ArcAβ models. DTI changes due to basal forebrain cholinergic neuron loss (Kerbler et al., 2013), or to a direct intracranial infusion of $A\beta_{1-42}$ (Sun et al., 2014) have also been shown. In general, these studies found reduced fractional anisotropy and increased mean and radial diffisivity in white matter, but also the reverse pattern has been presented, suggesting that different mechanisms can contribute opposite effects, or that sampling different time points can illustrate different stages of pathology. The observed heterogeneity may also be produced, in part, by abnomal brain maturation of the different mouse models (Qin et al., 2013; Grandjean et al., 2016). The most studied white matter tracts have been the corpus callosum, internal capsule (Müller et al., 2013; Qin et al., 2013), anterior commissure (Qin et al., 2013), and more rarely optic tracts (Sun et al., 2014). We also found lower FA in the internal capsule, and lower E1 in the optic tracts; and because we analyzed the whole brain, we identified several other tracts with altered diffusion properties, most prominently the fornix and hippocampus commissure, but also the cerebral and middle cerebellar peduncles. Compared to ROI-based approaches (Harms et al., 2006), our approach is hypothesis-free and has the potential to reveal morphometric and DTI changes throughout the brain, using high-resolution, isotropic imaging.

To further understand the underlying substrate for abnormalities detected by MR in the CVN-AD mouse, we used histology (LFB) and ultrastructural imaging (transmission electron microscopy [TEM]), and found them to support the evidence from DTI. Among the white matter tracts measured using light microscopy (LFB), only the fimbria showed reduced myelin content. TEM of the fornix provided striking evidence of white matter differences in CVN-AD mice. Our quantitative analysis revealed that the fornix had a lower density of myelinated axons, increased variability in diameter, and increased g-ratio, also indicative of myelin abnormalities. The presence of degenerating axoplasm, as well as lipofuscin, can be attributed to cellular death and neurodegeneration, while the presence of lysosomal bodies does not exclude direct glial attacks on myelin. This argument is supported by the observation of CD68-stained cells not only within the gray matter of the subiculum, hippocampus, and in proximity of the alveus, but also within the fimbria. While an exact mechanism cannot be determined by these techniques, the presence of highly phagocytic microglia in the same affected regions implies that microglia may be active participants in the removal of debris and perhaps, in the neurodegenerative process itself.

Together, our findings support the hypothesis that white mater dysfunction plays a role in AD, and we quantified differences in a mouse model of AD using multiple imaging methods, at different resolution scales, and in multivariate parameters within one modality (volume and DTI; or axonal density, diameters, and g-ratios). We demonstrated that morphometric and diffusion tensor parameters can detect white matter deficiencies, and conceivably, can be used to detect reversal/prevention of these disease-based parameters with treatment. Fiber tract disintegration and loss of connectivity has now been identified as a critical pathology in AD brain by multiple groups (Zhou et al., 2008; Damoiseaux et al., 2009; Cavedo et al., 2014; Cai et al., 2015; Mallio et al., 2015; Remy et al., 2015). Thus,

detecting the degree and extent of fiber tract disintegration using these non-invasive MRI techniques is likely to facilitate identification of early disease and progression and has been suggested as a reasonable functional biomarker of disease. However, the functional plasticity of the brain, the exact timing of pathological changes and the locations of affected tracts provide justifiable caution in the application of MRI tractography as an absolute indicator of onset or progression of AD pathology.

It is clear, however, that using this technique to model human disease has distinct limitations. Mice cannot perfectly model human AD, but can be used to help understand disease mechanisms. For example, CVN-AD mice aged 14–18 months model both Braak stages III to VI representative of AD, as well as a human age transitioning from advanced middle age towards senescence. Using CVN-AD mice at an approximately equivalent age and stage of disease, we were able to detect morphometric and microstructural changes in the hippocampus and its connecting fibers. Of particular interest was the septo-hippocampal circuit (the major cholinergic input to the hippocampus), because it plays a significant role in memory function, and is impaired in AD (Kasa et al., 1997). The fornix is a heavily myelinated tract, which connects the hippocampal formation with the septum, anterior thalamus, and hypothalamus. The precommissural fibers connect to interstitial nucleus of stria teminalis, accumbens, anterior olfactory nucleus, nucleus of the diagonal band, and preoptic areas, while postcommissural fibers connect to thalamus, hypothalamus, and midbrain (Insausti and Amaral 2004). Lesions of the fornix have disruptive effects on the connectivity of the hippocampus, and result in deficits in memory formation (Gupta et al., 2014; Dumont et al., 2015). We showed that structures along the SHH pathway have morphometric and microstructural alteration in the CVN-AD model, notably reduced FA, and that the fornix FA could be predicted by the hippocampal volume (R^2 ~0.6). Since microglia were present in the connecting fibers—the alveus and fimbria, which later feed into the fornix. The observed pathway changes can be explained, in part, by the interaction of reactive microglia with subicular and hippocampal gray matter. While not final proof, the combined histological and electron microscopy data strongly suggest that microglia in this region are phagocytic and contribute to the neuronal degeneration that accompanies the loss of myelin, and the changes in FA and RD. Further investigations are warranted to better understand the role of astrocytes in maintaining/repairing myelin (Nash et al., 2011; Barnett and Linington, 2013) in this mouse.

Although DTI provides great contrast for white matter fibers in FA images, further limitations to its use must be considered. For example, severe white matter pathology can reduce the accuracy of registration. The presence of enlarged axons and myelin debris can further bias the registration, leading to overestimating the volume of the corpus callosum, despite lower FA. While major phenotypes could be retrieved both from *in vivo* and *ex vivo* morphometry, there were also substantial differences. Both image sets identified atrophy of the olfactory areas, septum, hippocampus, and fornix, and hypertrophy of the isocortex and cerebellum. Two main differences come from the superior contrast (2.8 times higher contrast to noise between FA and T2 signal for the anterior commissure relative to septum) and resolution (6 times higher) in the *ex vivo* images compared to *in vivo*. These factors corroborate to increase the accuracy of definition for major gray matter structures, most of which are white matter bound. The strong image features help drive a more accurate

registration based on DTI, relative to our RARE *in vivo* images. However, fixation can cause shrinkage, or nonuniform filling of cerebrospinal fluid areas. We believe this later potential source of variability, leads to the loss of significance for the hypertrophy of the lateral ventricles in DTI images, which is however detected *in vivo*.

White matter integrity also depends on age, and TEM images revealed age-related abnormalities in both genotypes. Despite this, CVN-AD mice showed prevalence for disease. CVN-AD mice showed clear disease processes that were different from control mice within the same age groupings used in our experiments. However, we recognize that a tighter control over the age range may have reduced the variability in our measurements. Future efforts will be undertaken to separate normal aging from disease-associated changes, including using mice at younger ages. These additional studies should also allow us to better understand how age itself, is a major risk factor for Alzheimer's disease.

One limitation comes from the fact that our sample was small, and thus we could not examine gender effects. Such larger studies will become possible with the help of streamlined image analysis, implemented into a high-performance computing environment. Efficient pipelines will ensure reproducible procedures for animals of different ages, genders, or different models to help identify sensitive biomarkers, and assess their ability to track changes over time in imaging parameters, and their associations with behavior (Mielke et al., 2009). It will be interesting to follow not just disease progression, but also track the effectiveness of potential therapies targeting white matter (Holroyd et al., 2015).

Supplementary Material

Refer to Web version on PubMed Central for supplementary material.

Acknowledgments

We thank Dr. G Allan Johnson, Martin Fisher, Luke Xie, and Richard O'Brien for inspiring discussions, Michelle Plue, Dr. Sara Miller and Dominique Ferrarelli for help with electron microscopy, John Nouls for maintaining the 7T magnet, and James Cook and Lucy Upchurch for software and hardware support. The Center for In Vivo Microscopy is supported through NIH awards P41 EB015897 and 1S10OD010683-01 (to Dr. G Allan Johnson). We also gratefully acknowledge NIH support for our research through R01 AG045422 (Colton), and K01 AG041211 (Badea).

REFERENCES

Aggarwal M, Zhang J, Mori S. Magnetic resonance imaging-based mouse brain atlas and its applications. Methods in Molecular Biology. 2010:251–270.

Akiyama H, Barger S, Barnum S, Bradt B, Bauer J, Cole GM, Cooper NR, Eikelenboom P, Emmerling M, Fiebich BL, Finch CE, Frautschy S, Griffin WS, Hampel H, Hull M, Landreth G, Lue L, Mrak R, Mackenzie IR, McGeer PL, O'Banion MK, Pachter J, Pasinetti G, Plata-Salaman C, Rogers J, Rydel R, Shen Y, Streit W, Strohmeyer R, Tooyoma I, Van Muiswinkel FL, Veerhuis R, Walker D, Webster S, Wegrzyniak B, Wenk G, Wyss-Coray T. Inflammation and Alzheimer's disease. Neurobiol Aging. 2000; 21:383–421. [PubMed: 10858586]

Allemang-Grand R, Scholz J, Ellegood J, Cahill LS, Laliberte C, Fraser PE, Josselyn SA, Sled JG, Lerch JP. Altered brain development in an early-onset murine model of Alzheimer's disease. Neurobiol Aging. 2015; 36:638–647. [PubMed: 25311279]

Attems J, Yamaguchi H, Saido TC, Thal DR. Capillary CAA and perivascular Abeta-deposition: two distinct features of Alzheimer's disease pathology. J Neurol Sci. 2010; 299:155–162. [PubMed: 20850138]

Avants BB, Epstein CL, Grossman M, Gee JC. Symmetric diffeomorphic image registration with cross-correlation: evaluating automated labeling of elderly and neurodegenerative brain. Med Image Anal. 2008; 12:26–41. [PubMed: 17659998]

Avants BB, Tustison NJ, Stauffer M, Song G, Wu B, Gee JC. The Insight ToolKit image registration framework. Front Neuroinform. 2014; 8:44. [PubMed: 24817849]

Badea A, Ali-Sharief AA, Johnson GA. Morphometric analysis of the C57BL/6J mouse brain. Neuroimage. 2007; 37:683–693. [PubMed: 17627846]

Badea A, Gewalt S, Avants BB, Cook JJ, Johnson GA. Quantitative mouse brain phenotyping based on single and multispectral MR protocols. Neuroimage. 2012; 63:1633–1645. [PubMed: 22836174]

Barnett SC, Linington C. Myelination: do astrocytes play a role? Neuroscientist. 2013; 19:442–450. [PubMed: 23131748]

Bartzokis G. Age-related myelin breakdown: a developmental model of cognitive decline and Alzheimer's disease. Neurobiol Aging. 2004; 25:5–18. author reply 49–62. [PubMed: 14675724]

Bartzokis G, Cummings JL, Sultzer D, Henderson VW, Nuechterlein KH, Mintz J. White matter structural integrity in healthy aging adults and patients with Alzheimer disease: a magnetic resonance imaging study. Arch Neurol. 2003; 60:393–398. [PubMed: 12633151]

Bateman RJ, Xiong C, Benzinger TLS, Fagan AM, Goate A, Fox NC, Marcus DS, Cairns NJ, Xie X, Blazey TM, Holtzman DM, Santacruz A, Buckles V, Oliver A, Moulder K, Aisen PS, Ghetti B, Klunk WE, McDade E, Martins RN, Masters CL, Mayeux R, Ringman JM, Rossor MN, Schofield PR, Sperling RA, Salloway S, Morris JC. Clinical and biomarker changes in dominantly inherited Alzheimer's disease. New England Journal of Medicine. 2012; 367:795–804. [PubMed: 22784036]

Beach TG, Walker R, McGeer EG. Patterns of gliosis in Alzheimer's disease and aging cerebrum. Glia. 1989; 2:420–436. [PubMed: 2531723]

Benveniste H, Ma Y, Dhawan J, Gifford A, Smith SD, Feinstein I, Du C, Grant SC, Hof PR. Anatomical and functional phenotyping of mice models of Alzheimer's disease by MR microscopy. Annals of the New York Academy of Sciences. 2007:12–29.

Bozzali M, Falini A, Franceschi M, Cercignani M, Zuffi M, Scotti G, Comi G, Filippi M. White matter damage in Alzheimer's disease assessed in vivo using diffusion tensor magnetic resonance imaging. J Neurol Neurosurg Psychiatry. 2002; 72:742–746. [PubMed: 12023417]

Braak H, Braak E, Bohl J. Staging of alzheimer-related cortical destruction. European Neurology. 1993; 33:403–408. [PubMed: 8307060]

Brun A, Englund E. A white matter disorder in dementia of the Alzheimer type: a pathoanatomical study. Ann Neurol. 1986; 19:253–262. [PubMed: 3963770]

Cai S, Huang L, Zou J, Jing L, Zhai B, Ji G, von Deneen KM, Ren J, Ren A. Changes in thalamic connectivity in the early and late stages of amnestic mild cognitive impairment: a resting-state functional magnetic resonance study from ADNI. PLoS One. 2015; 10:e0115573. [PubMed: 25679386]

Calabrese E, Badea A, Watson C, Johnson GA. A quantitative magnetic resonance histology atlas of postnatal rat brain development with regional estimates of growth and variability. Neuroimage. 2013; 71:196–206. [PubMed: 23353030]

Cavedo E, Lista S, Khachaturian Z, Aisen P, Amouyel P, Herholz K, Jack CR Jr, Sperling R, Cummings J, Blennow K, O'Bryant S, Frisoni GB, Khachaturian A, Kivipelto M, Klunk W, Broich K, Andrieu S, de Schotten MT, Mangin JF, Lammertsma AA, Johnson K, Teipel S, Drzezga A, Bokde A, Colliot O, Bakardjian H, Zetterberg H, Dubois B, Vellas B, Schneider LS, Hampel H. The Road Ahead to Cure Alzheimer's Disease: Development of Biological Markers and Neuroimaging Methods for Prevention Trials Across all Stages and Target Populations. J Prev Alzheimers Dis. 2014; 1:181–202. [PubMed: 26478889]

Colton CA, Vitek MP, Wink DA, Xu Q, Cantillana V, Previti ML, Van Nostrand WE, Weinberg JB, Dawson H. NO synthase 2 (NOS2) deletion promotes multiple pathologies in a mouse model of Alzheimer's disease. Proc Natl Acad Sci U S A. 2006; 103:12867–12872. [PubMed: 16908860]

Colton CA, Wilson JG, Everhart A, Wilcock DM, Puolivali J, Heikkinen T, Oksman J, Jaaskelainen O, Lehtimaki K, Laitinen T, Vartiainen N, Vitek MP. mNos2 deletion and human NOS2 replacement in Alzheimer disease models. J Neuropathol Exp Neurol. 2014; 73:752–769. [PubMed: 25003233]

Copenhaver BR, Rabin LA, Saykin AJ, Roth RM, Wishart HA, Flashman LA, Santulli RB, McHugh TL, Mamourian AC. The fornix and mammillary bodies in older adults with Alzheimer's disease, mild cognitive impairment, and cognitive complaints: A volumetric MRI study. Psychiatry Research -Neuroimaging. 2006; 147:93–103. [PubMed: 16920336]

Damoiseaux JS, Smith SM, Witter MP, Sanz-Arigita EJ, Barkhof F, Scheltens P, Stam CJ, Zarei M, Rombouts SARB. White matter tract integrity in aging and alzheimer's disease. Human Brain Mapping. 2009; 30:1051–1059. [PubMed: 18412132]

Davis J, Xu F, Deane R, Romanov G, Previti ML, Zeigler K, Zlokovic BV, Van Nostrand WE. Early-onset and robust cerebral microvascular accumulation of amyloid beta-protein in transgenic mice expressing low levels of a vasculotropic Dutch/Iowa mutant form of amyloid beta-protein precursor. J Biol Chem. 2004; 279:20296–20306. [PubMed: 14985348]

di Penta A, Moreno B, Reix S, Fernandez-Diez B, Villanueva M, Errea O, Escala N, Vandenbroeck K, Comella JX, Villoslada P. Oxidative stress and proinflammatory cytokines contribute to demyelination and axonal damage in a cerebellar culture model of neuroinflammation. PLoS One. 2013; 8:e54722. [PubMed: 23431360]

Dickerson BC, Salat DH, Greve DN, Chua EF, Rand-Giovannetti E, Rentz DM, Bertram L, Mullin K, Tanzi RE, Blacker D, Albert MS, Sperling RA. Increased hippocampal activation in mild cognitive impairment compared to normal aging and AD. Neurology. 2005; 65:404–411. [PubMed: 16087905]

Douet V, Chang L. Fornix as an imaging marker for episodic memory deficits in healthy aging and in various neurological disorders. Front Aging Neurosci. 2015:7. [PubMed: 25762930]

Dumont JR, Amin E, Wright NF, Dillingham CM, Aggleton JP. The impact of fornix lesions in rats on spatial learning tasks sensitive to anterior thalamic and hippocampal damage. Behav Brain Res. 2015; 278:360–374. [PubMed: 25453745]

Eskildsen SF, Coupe P, Fonov VS, Pruessner JC, Collins DL. Structural imaging biomarkers of Alzheimer's disease: predicting disease progression. Neurobiol Aging. 2015; 36(Suppl 1):S23–31. [PubMed: 25260851]

Ewers M, Sperling RA, Klunk WE, Weiner MW, Hampel H. Neuroimaging markers for the prediction and early diagnosis of Alzheimer's disease dementia. Trends Neurosci. 2011; 34:430–442. [PubMed: 21696834]

Fortea J, Sala-Llonch R, Bartres-Faz D, Bosch B, Llado A, Bargallo N, Molinuevo JL, Sanchez-Valle R. Increased cortical thickness and caudate volume precede atrophy in PSEN1 mutation carriers. J Alzheimers Dis. 2010; 22:909–922. [PubMed: 20858974]

Fox, JGA. The Mouse in Biomedical Research [electronic resource]: History, Wild Mice, and Genetics. Elsevier Jan 2007 Ipswich. New York: Ebsco Publishing [Distributor]; 2007.

Friston KJ, Worsley KJ, Frackowiak RS, Mazziotta JC, Evans AC. Assessing the significance of focal activations using their spatial extent. Hum Brain Mapp. 1994; 1:210–220. [PubMed: 24578041]

Frodl T, Amico F. Is there an association between peripheral immune markers and structural/functional neuroimaging findings? Progress in Neuro-Psychopharmacology and Biological Psychiatry. 2014; 48:295–303. [PubMed: 23313563]

Gallivanone F, Della Rosa PA, Castiglioni I. Statistical Voxel-Based Methods and [18F]FDG PET Brain Imaging: Frontiers for the Diagnosis of AD. Curr Alzheimer Res. 2016; 13:682–694. [PubMed: 26567733]

Genovese CR, Lazar NA, Nichols T. Thresholding of statistical maps in functional neuroimaging using the false discovery rate. Neuroimage. 2002; 15:870–878. [PubMed: 11906227]

Gispert JD, Rami L, Sanchez-Benavides G, Falcon C, Tucholka A, Rojas S, Molinuevo JL. Nonlinear cerebral atrophy patterns across the Alzheimer's disease continuum: impact of APOE4 genotype. Neurobiol Aging. 2015; 36:2687–2701. [PubMed: 26239178]

Grand'Maison M, Zehntner SP, Ho MK, Hébert F, Wood A, Carbonell F, Zijdenbos AP, Hamel E, Bedell BJ. Early cortical thickness changes predict β-amyloid deposition in a mouse model of Alzheimer's disease. Neurobiology of Disease. 2013; 54:59–67. [PubMed: 23454197]

Grandjean J, Derungs R, Kulic L, Welt T, Henkelman M, Nitsch RM, Rudin M. Complex interplay between brain function and structure during cerebral amyloidosis in APP transgenic mouse strains revealed by multi-parametric MRI comparison. Neuroimage. 2016

Guo Z, Shao L, Zheng L, Du Q, Li P, John B, Geller DA. miRNA-939 regulates human inducible nitric oxide synthase posttranscriptional gene expression in human hepatocytes. Proc Natl Acad Sci U S A. 2012; 109:5826–5831. [PubMed: 22451906]

Gupta M, Kantor MA, Tung CE, Zhang N, Albers GW. Transient global amnesia associated with a unilateral infarction of the fornix: case report and review of the literature. Front Neurol. 2014; 5:291. [PubMed: 25628601]

Harms MP, Kotyk JJ, Merchant KM. Evaluation of white matter integrity in ex vivo brains of amyloid plaque-bearing APPsw transgenic mice using magnetic resonance diffusion tensor imaging. Exp Neurol. 2006; 199:408–415. [PubMed: 16483571]

Holroyd KB, Fosdick L, Smith GS, Leoutsakos JM, Munro CA, Oh ES, Drake KE, Rosenberg PB, Anderson WS, Salloway S, Pendergrass JC, Burke AD, Wolk DA, Tang-Wai DF, Ponce FA, Asaad WF, Sabbagh MN, Okun MS, Baltuch G, Foote KD, Targum SD, Lozano AM, Lyketsos CG. Deep brain stimulation targeting the fornix for mild Alzheimer dementia: Design of the ADvance randomized controlled trial. Open Access Journal of Clinical Trials. 2015; 7:63–76.

Hoos MD, Richardson BM, Foster MW, Everhart A, Thompson JW, Moseley MA, Colton CA. Longitudinal study of differential protein expression in an Alzheimer's mouse model lacking inducible nitric oxide synthase. J Proteome Res. 2013; 12:4462–4477. [PubMed: 24006891]

Hoos MD, Vitek MP, Ridnour LA, Wilson J, Jansen M, Everhart A, Wink DA, Colton CA. The impact of human and mouse differences in NOS2 gene expression on the brain's redox and immune environment. Mol Neurodegener. 2014; 9:50. [PubMed: 25403885]

Iacono D, O'Brien R, Resnick SM, Zonderman AB, Pletnikova O, Rudow G, An Y, West MJ, Crain B, Troncoso JC. Neuronal hypertrophy in asymptomatic Alzheimer disease. J Neuropathol Exp Neurol. 2008; 67:578–589. [PubMed: 18520776]

Ihara M, Polvikoski TM, Hall R, Slade JY, Perry RH, Oakley AE, Englund E, O'Brien JT, Ince PG, Kalaria RN. Quantification of myelin loss in frontal lobe white matter in vascular dementia, Alzheimer's disease, and dementia with Lewy bodies. Acta Neuropathol. 2010; 119:579–589. [PubMed: 20091409]

Insausti, R.; Amaral, DG. The hippocampal formation. In: Paxinos, G.; Mai, J., editors. The Human Nervous System. Elsevier; 2004. p. 871-914.

Jack CR Jr, Petersen RC, Xu YC, O'Brien PC, Smith GE, Ivnik RJ, Boeve BF, Waring SC, Tangalos EG, Kokmen E. Prediction of AD with MRI-based hippocampal volume in mild cognitive impairment. Neurology. 1999; 52:1397–1403. [PubMed: 10227624]

Jack CR Jr, Petersen RC, Xu YC, Waring SC, O'Brien PC, Tangalos EG, Smith GE, Ivnik RJ, Kokmen E. Medial temporal atrophy on MRI in normal aging and very mild Alzheimer's disease. Neurology. 1997; 49:786–794. [PubMed: 9305341]

Jack CR Jr, Wiste HJ, Weigand SD, Knopman DS, Mielke MM, Vemuri P, Lowe V, Senjem ML, Gunter JL, Reyes D, Machulda MM, Roberts R, Petersen RC. Different definitions of neurodegeneration produce similar amyloid/neurodegeneration biomarker group findings. Brain. 2015; 138:3747–3759. [PubMed: 26428666]

Jack CR Jr, Petersen RC, Xu YC, O'Brien PC, Smith GE, Ivnik RJ, Boeve BF, Waring SC, Tangalos EG, Kokmen E. Prediction of AD with MRI-based hippocampal volume in mild cognitive impairment. Neurology. 1999; 52:1397–1403. [PubMed: 10227624]

Jack CR Jr, Petersen RC, Xu YC, Waring SC, O'Brien PC, Tangalos EG, Smith GE, Ivnik RJ, Kokmen E. Medial temporal atrophy on MRI in normal aging and very mild Alzheimer's disease. Neurology. 1997; 49:786–794. [PubMed: 9305341]

Johnson GA, Ali-Sharief A, Badea A, Brandenburg J, Cofer G, Fubara B, Gewalt S, Hedlund LW, Upchurch L. High-throughput morphologic phenotyping of the mouse brain with magnetic resonance histology. Neuroimage. 2007; 37:82–89. [PubMed: 17574443]

Johnson GA, Badea A, Brandenburg J, Cofer G, Fubara B, Liu S, Nissanov J. Waxholm space: an image-based reference for coordinating mouse brain research. Neuroimage. 2010; 53:365–372. [PubMed: 20600960]

Johnson GA, Cofer GP, Gewalt SL, Hedlund LW. Morphologic phenotyping with MR microscopy: the visible mouse. Radiology. 2002; 222:789–793. [PubMed: 11867802]

Ka¨rkka¨inen E, Lahtinen HM, Na¨rva¨inen J, Gröhn O, Tanila H. Brain Amyloidosis and BDNF Deficiency Have Opposite Effects on Brain Volumes in AβPP/PS1 Mice Both in vivo and ex vivo. Journal of Alzheimer's Disease. 2015; 46:929–946.

Kan MJ, Lee JE, Wilson JG, Everhart AL, Brown CM, Hoofnagle AN, Jansen M, Vitek MP, Gunn MD, Colton CA. Arginine Deprivation and Immune Suppression in a Mouse Model of Alzheimer's Disease. The Journal of Neuroscience. 2015; 35:5969–5982. [PubMed: 25878270]

Kantarci K, Weigand SD, Przybelski SA, Shiung MM, Whitwell JL, Negash S, Knopman DS, Boeve BF, O'Brien PC, Petersen RC, Jack CR. Risk of dementia in MCI: Combined effect of cerebrovascular disease, volumetric MRI, and 1H MRS. Neurology. 2009; 72:1519–1525. [PubMed: 19398707]

Kasa P, Rakonczay Z, Gulya K. The cholinergic system in Alzheimer's disease. Prog Neurobiol. 1997; 52:511–535. [PubMed: 9316159]

Kerbler GM, Hamlin AS, Pannek K, Kurniawan ND, Keller MD, Rose SE, Coulson EJ. Diffusion-weighted magnetic resonance imaging detection of basal forebrain cholinergic degeneration in a mouse model. Neuroimage. 2013; 66:133–141. [PubMed: 23128077]

Kovačević N, Henderson JT, Chan E, Lifshitz N, Bishop J, Evans AC, Henkelman RM, Chen XJ. A three-dimensional MRI atlas of the mouse brain with estimates of the average and variability. Cerebral Cortex. 2005; 15:639–645. [PubMed: 15342433]

Laubach VE, Foley PL, Shockey KS, Tribble CG, Kron IL. Protective roles of nitric oxide and testosterone in endotoxemia: evidence from NOS-2-deficient mice. Am J Physiol. 1998; 275:H2211–2218. [PubMed: 9843821]

Mallio CA, Schmidt R, de Reus MA, Vernieri F, Quintiliani L, Curcio G, Beomonte Zobel B, Quattrocchi CC, van den Heuvel MP. Epicentral disruption of structural connectivity in Alzheimer's disease. CNS Neurosci Ther. 2015; 21:837–845. [PubMed: 25899584]

Miao J, Xu F, Davis J, Otte-Holler I, Verbeek MM, Van Nostrand WE. Cerebral microvascular amyloid beta protein deposition induces vascular degeneration and neuroinflammation in transgenic mice expressing human vasculotropic mutant amyloid beta precursor protein. Am J Pathol. 2005; 167:505–515. [PubMed: 16049335]

Mielke MM, Kozauer NA, Chan KCG, George M, Toroney J, Zerrate M, Bandeen-Roche K, Wang MC, vanZijl P, Pekar JJ, Mori S, Lyketsos CG, Albert M. Regionally-specific diffusion tensor imaging in mild cognitive impairment and Alzheimer's disease. Neuroimage. 2009; 46:47–55. [PubMed: 19457371]

Minoshima S, Giordani B, Berent S, Frey KA, Foster NL, Kuhl DE. Metabolic reduction in the posterior cingulate cortex in very early Alzheimer's disease. Ann Neurol. 1997; 42:85–94. [PubMed: 9225689]

Müller HP, Kassubek J, Vernikouskaya I, Ludolph AC, Stiller D, Rasche V. Diffusion Tensor Magnetic Resonance Imaging of the Brain in APP Transgenic Mice: A Cohort Study. PLoS One. 2013:8.

Nash B, Thomson CE, Linington C, Arthur AT, McClure JD, McBride MW, Barnett SC. Functional duality of astrocytes in myelination. J Neurosci. 2011; 31:13028–13038. [PubMed: 21917786]

Nowrangi MA, Rosenberg PB. The fornix in mild cognitive impairment and Alzheimer's disease. Front Aging Neurosci. 2015; 7:1. [PubMed: 25653617]

Oddo S, Caccamo A, Shepherd JD, Murphy MP, Golde TE, Kayed R, Metherate R, Mattson MP, Akbari Y, LaFerla FM. Triple-transgenic model of Alzheimer's disease with plaques and tangles: intracellular Abeta and synaptic dysfunction. Neuron. 2003; 39:409–421. [PubMed: 12895417]

Oishi K, Lyketsos CG. Alzheimer's disease and the fornix. Front Aging Neurosci. 2014; 6:241. [PubMed: 25309426]

Ottnad E, Parthasarathy S, Sambrano GR, Ramprasad MP, Quehenberger O, Kondratenko N, Green S, Steinberg D. A macrophage receptor for oxidized low density lipoprotein distinct from the receptor for acetyl low density lipoprotein: partial purification and role in recognition of oxidatively damaged cells. Proc Natl Acad Sci U S A. 1995; 92:1391–1395. [PubMed: 7533292]

Parra MA, Saarimäki H, Bastin ME, Londoño AC, Pettit L, Lopera F, Della Sala S, Abrahams S. Memory binding and white matter integrity in familial Alzheimer's disease. Brain. 2015; 138:1355–1369. [PubMed: 25762465]

Pathak AP, Kim E, Zhang J, Jones MV. Three-Dimensional imaging of the mouse neurovasculature with magnetic resonance microscopy. PLoS One. 2011:6.

Paxinos, G.; Franklin, K. The Mouse Brain in Stereotaxic Coordinates. 4th. San Diego: Academic Press, Elsevier; 2013.

Qin YY, Li MW, Zhang S, Zhang Y, Zhao LY, Lei H, Oishi K, Zhu WZ. In vivo quantitative whole-brain diffusion tensor imaging analysis of APP/PS1 transgenic mice using voxel-based and atlas-based methods. Neuroradiology. 2013; 55:1027–1038. [PubMed: 23644540]

Ramprasad MP, Terpstra V, Kondratenko N, Quehenberger O, Steinberg D. Cell surface expression of mouse macrosialin and human CD68 and their role as macrophage receptors for oxidized low density lipoprotein. Proc Natl Acad Sci U S A. 1996; 93:14833–14838. [PubMed: 8962141]

Remy F, Vayssiere N, Saint-Aubert L, Barbeau E, Pariente J. White matter disruption at the prodromal stage of Alzheimer's disease: relationships with hippocampal atrophy and episodic memory performance. Neuroimage Clin. 2015; 7:482–492. [PubMed: 25685715]

Ringman JM, O'Neill J, Geschwind D, Medina L, Apostolova LG, Rodriguez Y, Schaffer B, Varpetian A, Tseng B, Ortiz F, Fitten J, Cummings JL, Bartzokis G. Diffusion tensor imaging in preclinical and presymptomatic carriers of familial Alzheimer's disease mutations. Brain. 2007; 130:1767–1776. [PubMed: 17522104]

Schneider CA, Rasband WS, Eliceiri KW. NIH Image to ImageJ: 25 years of image analysis. Nat Methods. 2012; 9:671–675. [PubMed: 22930834]

Schott JM, Revesz T. Inflammation in Alzheimer's disease: insights from immunotherapy. Brain. 2013; 136:2654–2656. [PubMed: 23983027]

Shineman DW, Basi GS, Bizon JL, Colton CA, Greenberg BD, Hollister BA, Lincecum J, Leblanc GG, Lee LB, Luo F, Morgan D, Morse I, Refolo LM, Riddell DR, Scearce-Levie K, Sweeney P, Yrjanheikki J, Fillit HM. Accelerating drug discovery for Alzheimer's disease: best practices for preclinical animal studies. Alzheimers Res Ther. 2011; 3:28. [PubMed: 21943025]

Song SK, Kim JH, Lin SJ, Brendza RP, Holtzman DM. Diffusion tensor imaging detects age-dependent white matter changes in a transgenic mouse model with amyloid deposition. Neurobiology of Disease. 2004; 15:640–647. [PubMed: 15056472]

Sperling R. Functional MRI studies of associative encoding in normal aging, mild cognitive impairment, and Alzheimer's disease. Annals of the New York Academy of Sciences. 2007:146–155. [PubMed: 17413017]

Sperling RA, Aisen PS, Beckett LA, Bennett DA, Craft S, Fagan AM, Iwatsubo T, Jack CR Jr, Kaye J, Montine TJ, Park DC, Reiman EM, Rowe CC, Siemers E, Stern Y, Yaffe K, Carrillo MC, Thies B, Morrison-Bogorad M, Wagster MV, Phelps CH. Toward defining the preclinical stages of Alzheimer's disease: recommendations from the National Institute on Aging-Alzheimer's Association workgroups on diagnostic guidelines for Alzheimer's disease. Alzheimers Dement. 2011; 7:280–292. [PubMed: 21514248]

Sun SW, Liang HF, Mei J, Xu D, Shi WX. In vivo diffusion tensor imaging of amyloid-β-induced white matter damage in mice. Journal of Alzheimer's Disease. 2014; 38:93–101.

Sun SW, Song SK, Harms MP, Lin SJ, Holtzman DM, Merchant KM, Kotyk JJ. Detection of age-dependent brain injury in a mouse model of brain amyloidosis associated with Alzheimer's disease using magnetic resonance diffusion tensor imaging. Experimental Neurology. 2005; 191:77–85. [PubMed: 15589514]

Tan J, Town T, Paris D, Mori T, Suo Z, Crawford F, Mattson MP, Flavell RA, Mullan M. Microglial activation resulting from CD40-CD40l interaction after β-amyloid stimulation. Science. 1999; 286:2352–2355. [PubMed: 10600748]

Tustison NJ, Avants BB, Cook PA, Zheng Y, Egan A, Yushkevich PA, Gee JC. N4ITK: improved N3 bias correction. IEEE Trans Med Imaging. 2010; 29:1310–1320. [PubMed: 20378467]

Ullmann JFP, Janke AL, Reutens D, Watson C. Development of MRI-based atlases of non-human brains. Journal of Comparative Neurology. 2015; 523:391–405. [PubMed: 25236843]

Villain N, Desgranges B, Viader F, de la Sayette V, Mezenge F, Landeau B, Baron JC, Eustache F, Chetelat G. Relationships between hippocampal atrophy, white matter disruption, and gray matter hypometabolism in Alzheimer's disease. J Neurosci. 2008; 28:6174–6181. [PubMed: 18550759]

Vos SJ, Gordon BA, Su Y, Visser PJ, Holtzman DM, Morris JC, Fagan AM, Benzinger TL. NIA-AA staging of preclinical Alzheimer disease: discordance and concordance of CSF and imaging biomarkers. Neurobiol Aging. 2016; 44:1–8. [PubMed: 27318129]

Wang R, Benner T, Sorensen AG, Wedeen VJ. Diffusion Toolkit: A Software Package for Diffusion Imaging Data Processing and Tractography Proc. Intl. Soc. Mag. Reson. Med. 2007:3720.

Weinberg JB, Misukonis MA, Shami PJ, Mason SN, Sauls DL, Dittman WA, Wood ER, Smith GK, McDonald B, Bachus KE, et al. Human mononuclear phagocyte inducible nitric oxide synthase (iNOS): analysis of iNOS mRNA, iNOS protein, biopterin, and nitric oxide production by blood monocytes and peritoneal macrophages. Blood. 1995; 86:1184–1195. [PubMed: 7542498]

Wells JA, O'Callaghan JM, Holmes HE, Powell NM, Johnson RA, Siow B, Torrealdea F, Ismail O, Walker-Samuel S, Golay X, Rega M, Richardson S, Modat M, Cardoso MJ, Ourselin S, Schwarz AJ, Ahmed Z, Murray TK, O'Neill MJ, Collins EC, Colgan N, Lythgoe MF. In vivo imaging of tau pathology using multi-parametric quantitative MRI. Neuroimage. 2015; 111:369–378. [PubMed: 25700953]

Wilcock DM, Lewis MR, Van Nostrand WE, Davis J, Previti ML, Gharkholonarehe N, Vitek MP, Colton CA. Progression of amyloid pathology to Alzheimer's disease pathology in an amyloid precursor protein transgenic mouse model by removal of nitric oxide synthase 2. J Neurosci. 2008; 28:1537–1545. [PubMed: 18272675]

Wisniewski KE, Wisniewski HM, Wen GY. Occurrence of neuropathological changes and dementia of Alzheimer's disease in Down's syndrome. Annals of Neurology. 1985; 17:278–282. [PubMed: 3158266]

Worsley KJ, Evans AC, Marrett S, Neelin P. A three-dimensional statistical analysis for CBF activation studies in human brain. J Cereb Blood Flow Metab. 1992; 12:900–918. [PubMed: 1400644]

Xu Y, Jack CR Jr, O'Brien PC, Kokmen E, Smith GE, Ivnik RJ, Boeve BF, Tangalos RG, Petersen RC. Usefulness of MRI measures of entorhinal cortex versus hippocampus in AD. Neurology. 2000; 54:1760–1767. [PubMed: 10802781]

Yoshiyama Y, Higuchi M, Zhang B, Huang SM, Iwata N, Saido T, Maeda J, Suhara T, Trojanowski JQ, Lee VMY. Synapse Loss and Microglial Activation Precede Tangles in a P301S Tauopathy Mouse Model. Neuron. 2007; 53:337–351. [PubMed: 17270732]

Zhou Y, Dougherty JH Jr, Hubner KF, Bai B, Cannon RL, Hutson RK. Abnormal connectivity in the posterior cingulate and hippocampus in early Alzheimer's disease and mild cognitive impairment. Alzheimer's and Dementia. 2008; 4:265–270.

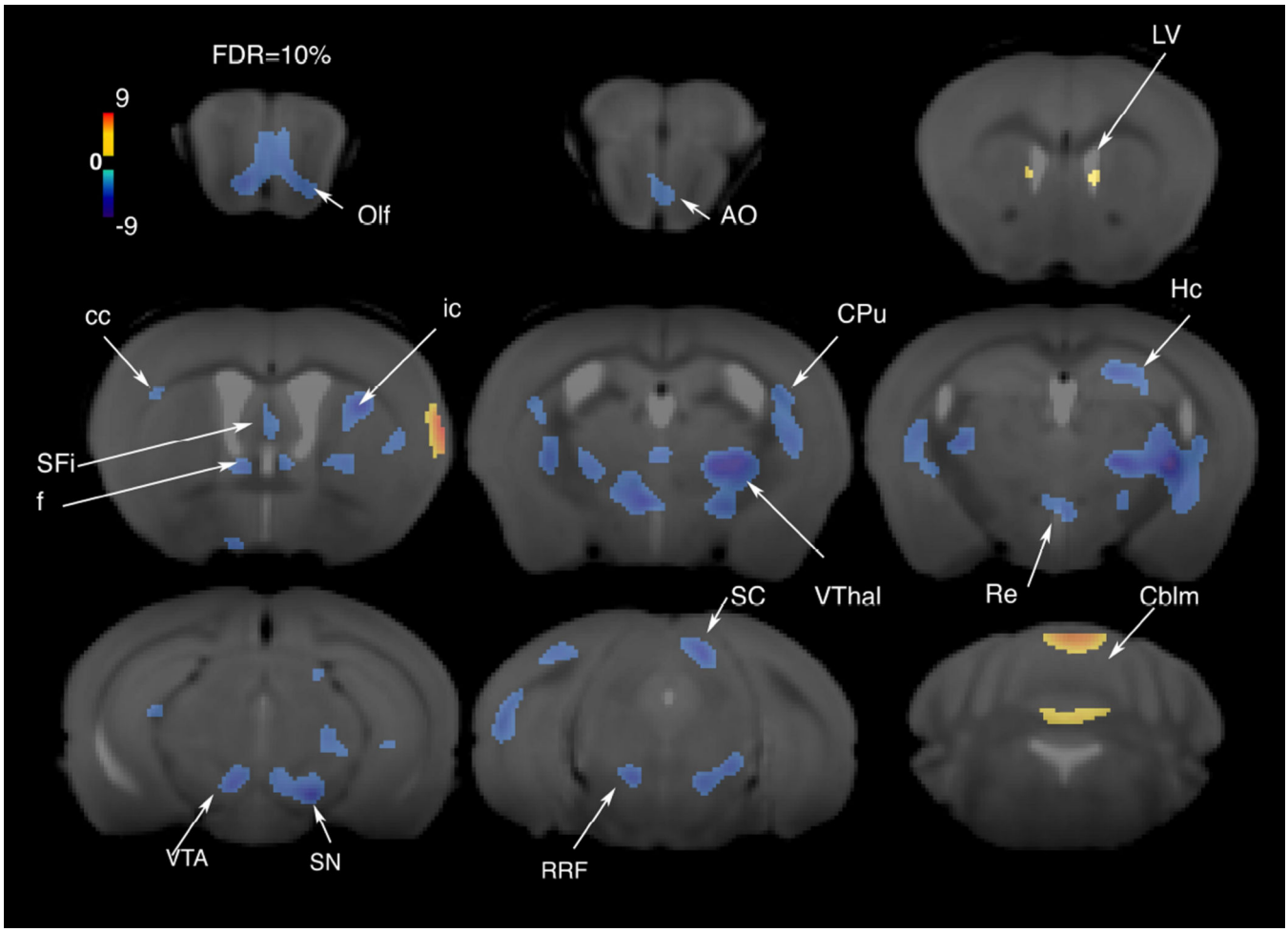

Figure 1. ***In vivo*** **MRI identified focal volume changes, including reduced fornix and septohippocampal areas (t maps of the log Jacobian for deformation fields, thresholded at FDR=10%, unitless)**

Regions of the neocortex (S1/S2) and cerebellum were enlarged, whereas olfactory regions, basal ganglia, thalamus, ventral tegmentum, and superior colliculus were reduced. Lateral ventricles appeared enlarged. *Abbreviations*: AO: accessory olfactory; CPu: caudate putamen; Cblm: cerebellum; Hc: hippocampus; Olf: olfactory; Re: reuniens thalamic nucleus; RRF: retrorubral field; SFi: septofimbrial nucleus; SC: superior colliculus; SN: substantia nigra; VTA: ventral tegmental area; VThal: ventral thalamus; f: fornix; ic: internal capsule; cc: corpus callosum.

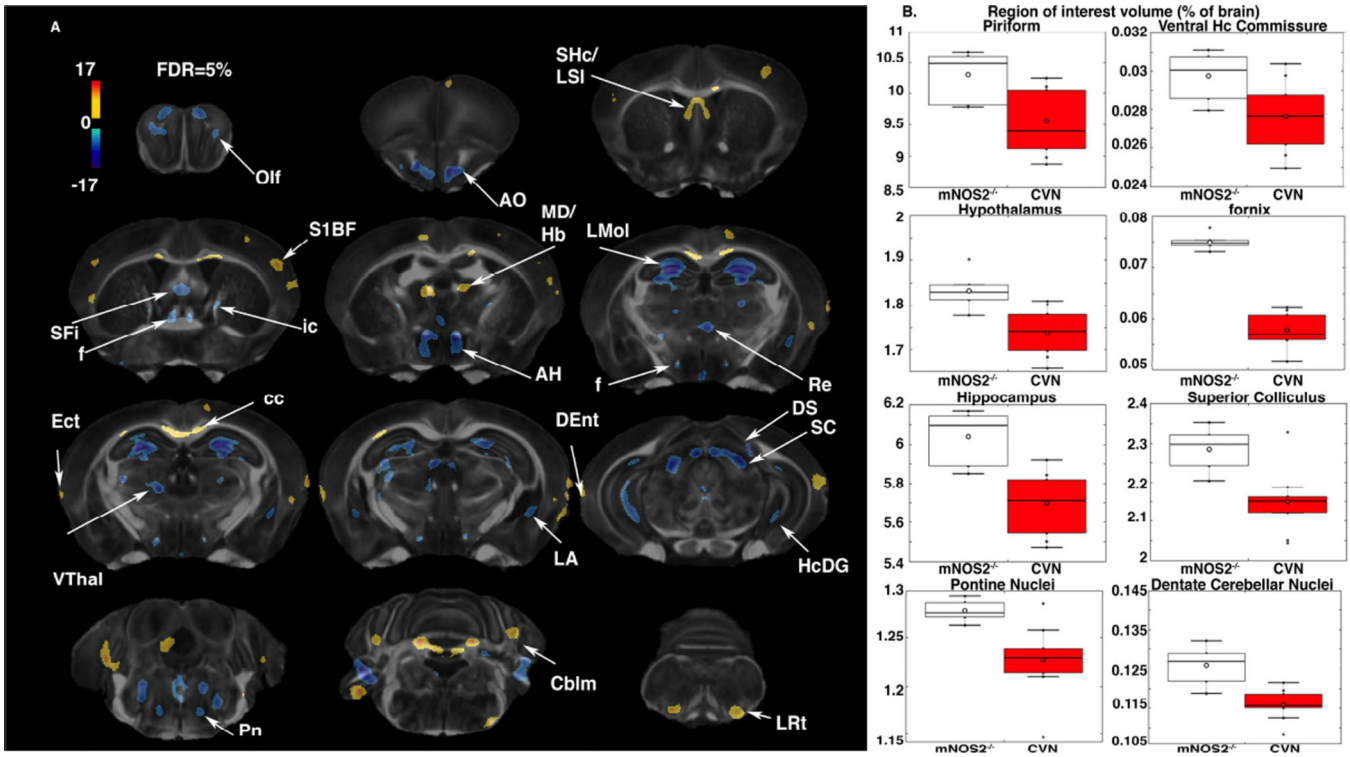

Figure 2. ***Ex vivo*** **DTI identified significant local volume differences in CVN-AD mice relative to controls (t maps, thresholded at FDR= 5%, unitless)**

Atrophy was observed in the olfactory areas, preoptic, hypothalamus, lateral amygdala, hippocampal commissure, septofimbrial nucleus, triangular septum, hippocampus, subiculum, ventral thalamic nuclei, superior colliculus, and pons, as well as the fornix and internal capsule. Areas of hypertrophy included the somatosensory cortex, corpus callosum (medially, and periventricular), dorsal thalamus, baso-medial amygdala, cerebellum (lobule 10), and the lateral reticular nucleus. (B) Volumes for selected regions of interest in both genotypes. Data are presented as medians (line), mean (circle), quantile (box, 25–75% of data range), range (whiskers). Abbreviations: AD: anterodorsal thalamic nuclei; AO: anterior olfactory; DEnt: dorsolateral entorhinal cortex; DS: dorsal subiculum; Ect: ectorhinal cortex; HcDG: dentate gyrus of hippocampus; LDDM: latero-dorsal thalamic nucleus (dorsomedial); LA: lateral amygdala; LRt: lateral reticular nucleus; LSI: lateral septal nucleus, intermediate part; LMol: lacunosum moleculare layer of the hippocampus; Olf: olfactory; Pn: pons; SC: superior colliculus; SFi: septofimbrial nucleus; cc: corpus callosum; f: fornix; ic: internal capsule.

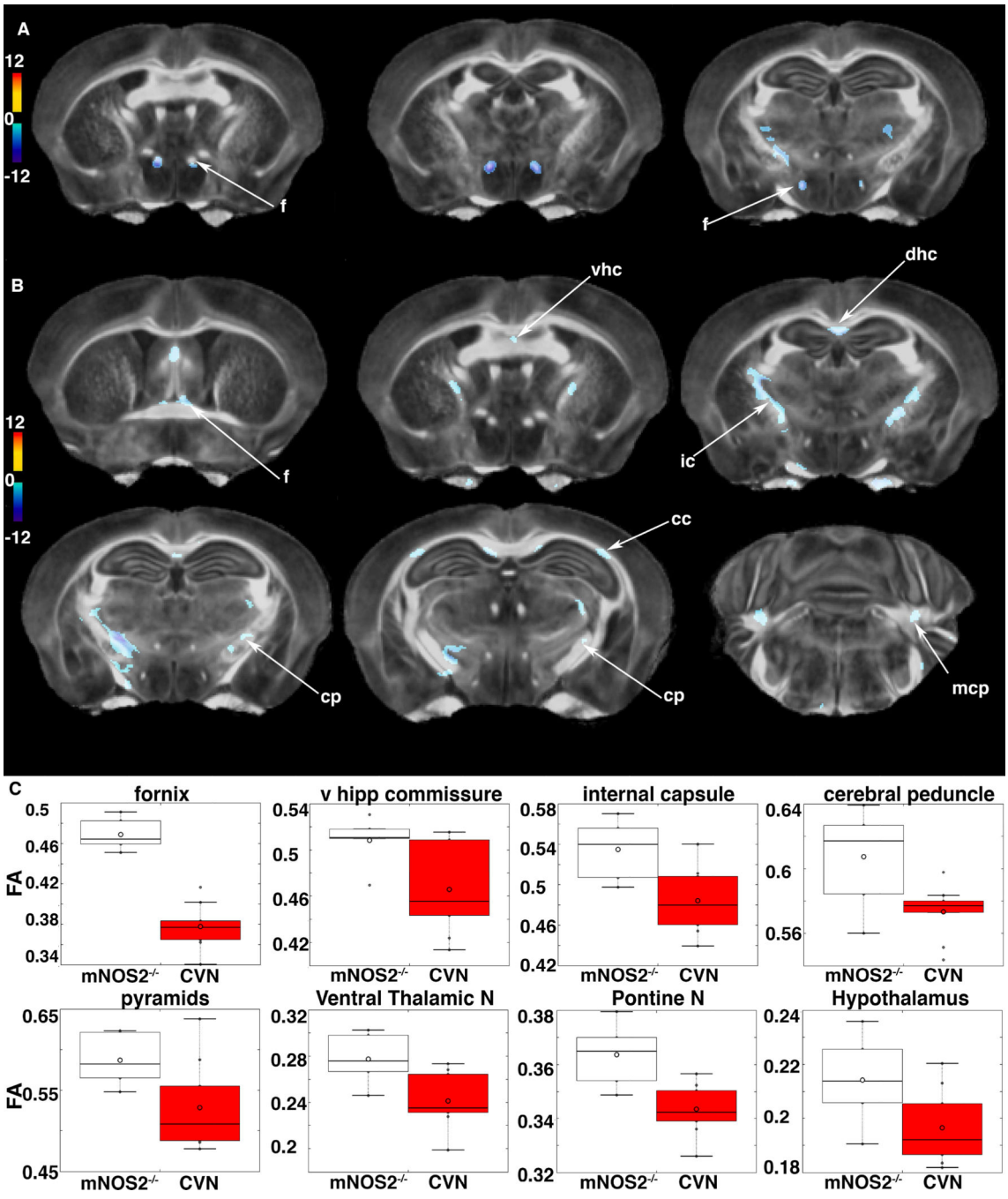

Figure 3. Fractional anisotropy (FA) differences between CVN-AD and *mNos2*$^{-/-}$ controls (t statistics, thresholded at FDR=5%, unitless)

(A) For a mask including the whole brain we observed a strong effect for the fornix, and within the thalamus only. (B) Restricting the mask to white matter (FA > 0.3), we found significant reductions in the fornix, corpus callosum, and internal capsule, as well as in cerebral peduncle, and middle cerebellar peduncle. (C) ROI based differences in FA. *Abbreviations:* cc: corpus callosum; cp: cerebral peduncle; dhc (vhc): dorsal (ventral) hippocampal commissure; ic: internal capsule; f: fornix; mcp: middle cerebellar peduncle.

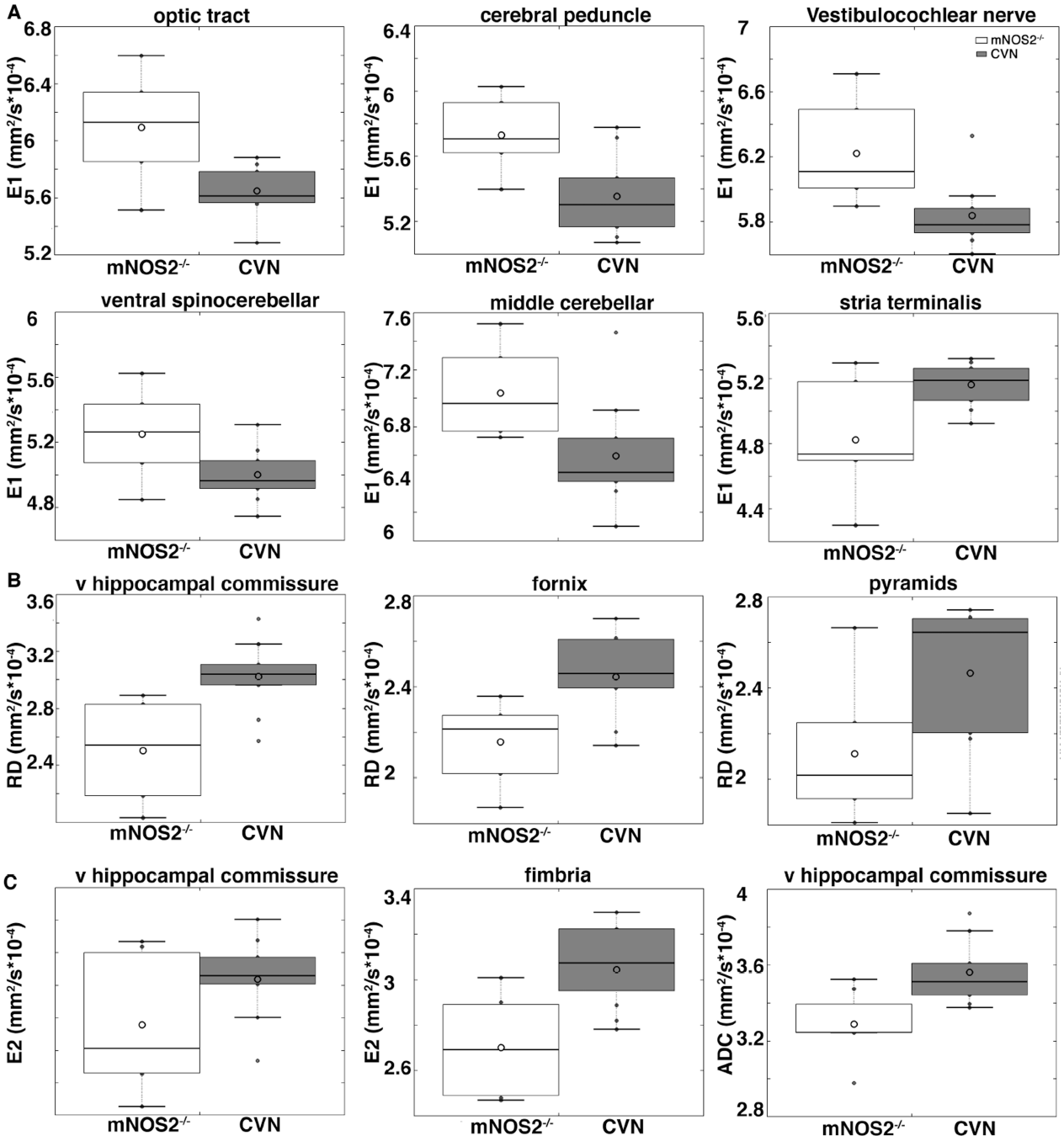

Figure 4. DTI multiparameter changes in CVN-AD mice (t statistics thresholded at p<0.05)

A) Axial diffusivity changes (E1, associated with axonal density) were significantly decreased in the optic tract, cerebral peduncle, vestibulocochlear nerve (n8), ventral spinocerebellar tract, and middle cerebellar peduncle (~7%), and increased in stria terminalis (which did not survive permutation corrections). B) Radial diffusivity (RD) associated with myelination) was significantly increased in several white mater tracts and pontine areas ($p<0.05$). The fornix, and hippocampal commissure were >10% increased. The difference for fimbria, corpus callosum, anterior commissure and brachium of the superior colliculus

showed a trend ($p<0.1$). c) Secondary eigenvalues changes and ADC point to the ventral hippocampal commissure and fimbria.

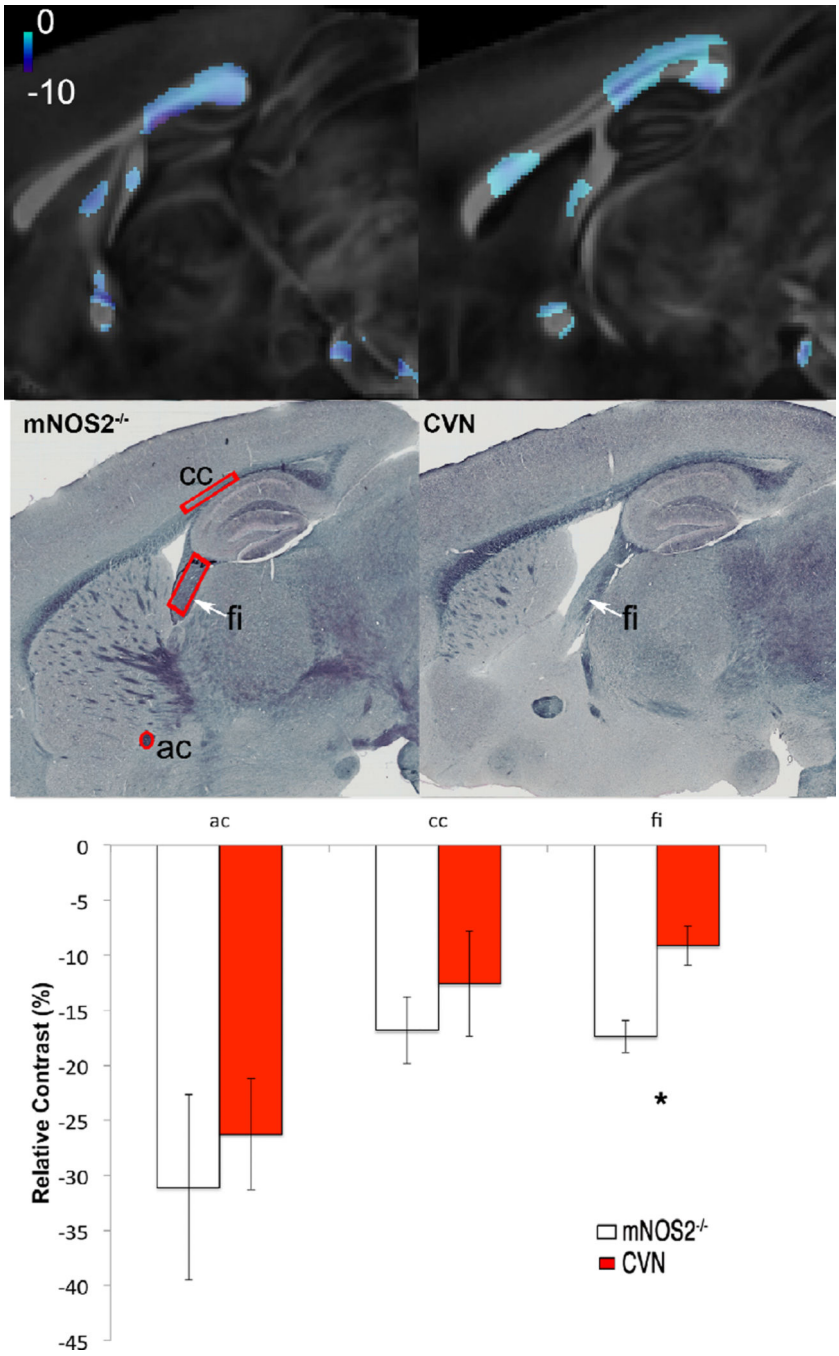

Figure 5. Decreased myelin content in the fimbria of CVN-AD mice was detected through luxol fast blue image contrast relative to the cortex for three regions of interest (fi: fimbria, cc: corpus callosum, ac: anterior commissure) indicated (d=-3.6, 8% contrast difference, p<0.01).

Data are presented in contrast to similar sections through the MR, where FA reductions are shown in blue; and as mean ± standard error of the mean. N = 4 animals/group.

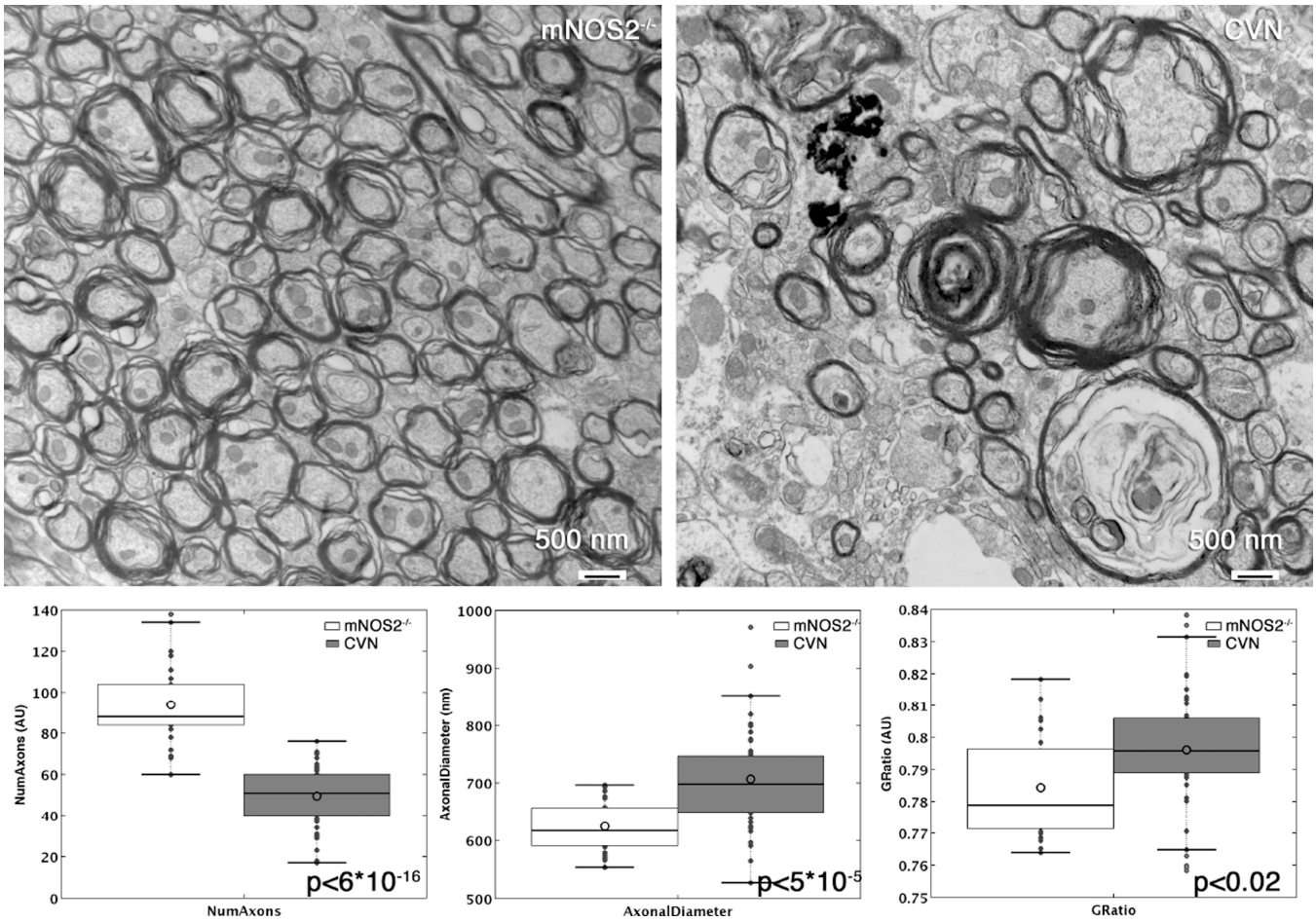

Figure 6. Representative transmission electron microscopy images through the fornix are indicative of abnormal white matter in CVN-AD mice (7100 x magnification)

Lower density of myelinated axons, increased variability in axonal size and shape, as well as enlarged G ratios, were found in CVN-AD mice compared to mNos2$^{-/-}$ control mice. Abnormalities of myelination were more frequently seen in CVN mice, and included ballooning, abnormal lamellation, and myelin figures in degenerated axons.

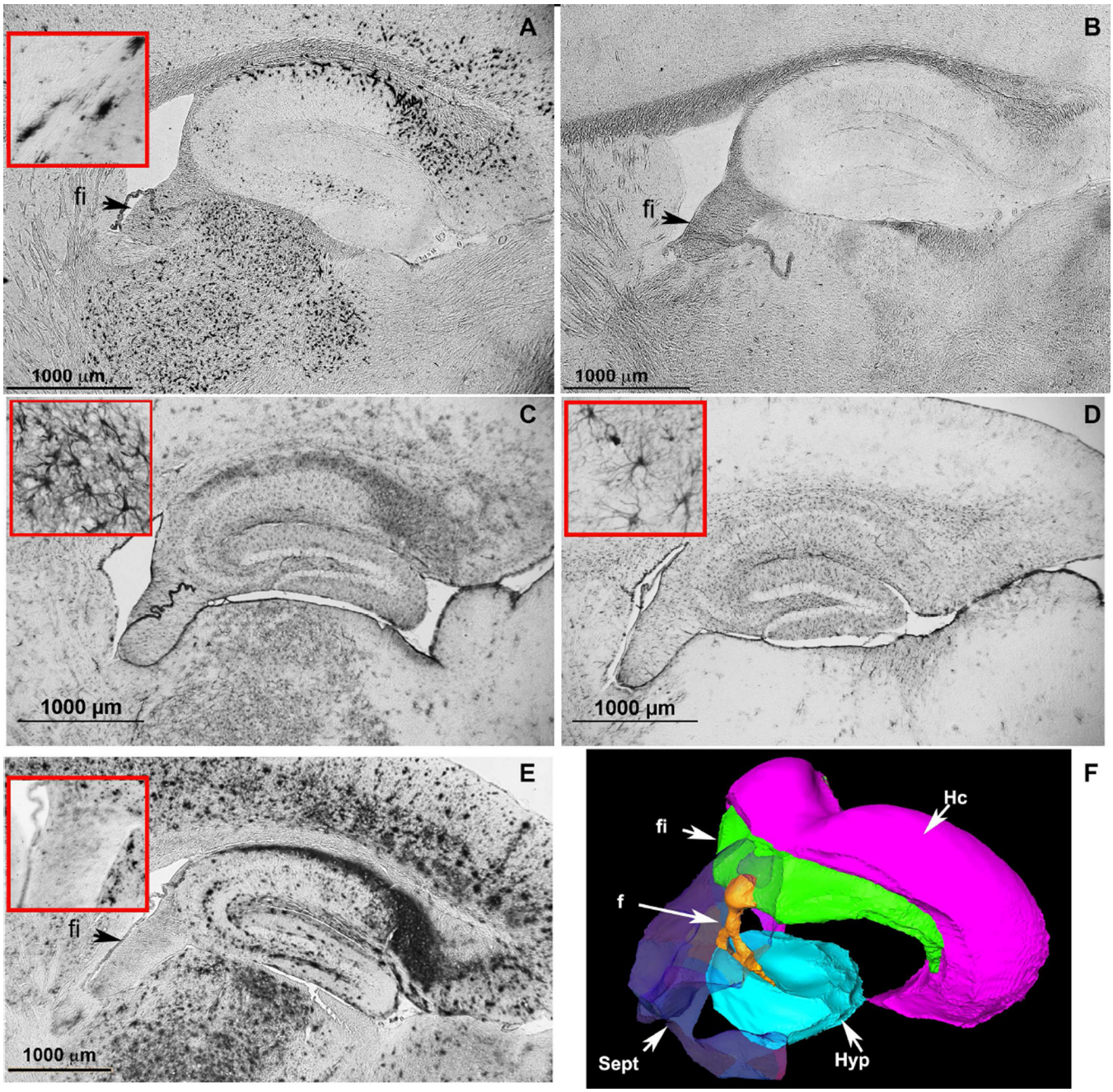

Figure 7. Several vulnerable areas identified by morphometric and/or DTI changes also stained for reactive microglia in CVN-AD mice, but not in controls

In particular areas of the hippocampus (CA1, CA3), as well as its connections - fimbria and alveus (A) stained for CD 68 (phagocytic marker) in CVN-AD mice (A), but not in controls (B). GFAP staining also revealed higher density and darker staining for reactive astrocytes in CVN mice (C) than in controls (D). In contrast Abeta staining was mostly found in gray matter areas, and not in the fimbria white matter, and only in CVN mice (E), but not on

controls. The structures involved are part of a circuitry known to be involved in human AD (fx: fornix, fi: fimbria, Hc: hippocampus; Hyp: hypothalamus) (F).